

## SUPERNOVA REMNANT PROGENITOR MASSES IN M31

ZACHARY G. JENNINGS<sup>1</sup>, BENJAMIN F. WILLIAMS<sup>1</sup>, JEREMIAH W. MURPHY<sup>2</sup>, JULIANNE J. DALCANTON<sup>1</sup>, KAROLINE M. GILBERT<sup>1,4</sup>, ANDREW E. DOLPHIN<sup>3</sup>, MORGAN FOUESNEAU<sup>1</sup>, DANIEL R. WEISZ<sup>1</sup>

*Draft version October 18, 2018*

### ABSTRACT

Using Hubble Space Telescope (HST) photometry, we age-date 59 supernova remnants (SNRs) in the spiral galaxy M31 and use these ages to estimate zero-age main sequence masses ( $M_{\text{ZAMS}}$ ) for their progenitors. To accomplish this, we create color-magnitude diagrams (CMDs) and employ CMD fitting to measure the recent star formation history (SFH) of the regions surrounding cataloged SNR sites. We identify any young coeval population that likely produced the progenitor star, then assign an age and uncertainty to that population. Application of stellar evolution models allows us to infer the  $M_{\text{ZAMS}}$  from this age. Because our technique is not contingent on identification or precise location of the progenitor star, it can be applied to the location of any known SNR. We identify significant young star formation around 53 of the 59 SNRs and assign progenitor masses to these, representing a factor of  $\sim 2$  increase over currently measured progenitor masses. We consider the remaining 6 SNRs as either probable Type Ia candidates or the result of core-collapse progenitors that have escaped their birth sites. In general, the distribution of recovered progenitor masses is bottom heavy, showing a paucity of the most massive stars. If we assume a single power law distribution,  $dN/dM \propto M^\alpha$ , we find a distribution that is steeper than a Salpeter IMF ( $\alpha = -2.35$ ). In particular, we find values of  $\alpha$  outside the range  $-2.7 \geq \alpha \geq -4.4$  to be inconsistent with our measured distribution at 95% confidence. If instead we assume a distribution that follows a Salpeter IMF up to some maximum mass, we find that values of  $M_{\text{Max}} > 26$  are inconsistent with the measured distribution at 95% confidence. In either scenario, the data suggest that some fraction of massive stars may not explode. The result is preliminary and requires more SNRs and further analysis. In addition, we use our distribution to estimate a minimum mass for core collapse between 7.0 and 7.8  $M_\odot$ .

*Subject headings:* galaxies:individual:(M31) — supernovae: general

### 1. INTRODUCTION

Both theoretically and observationally, core-collapse supernova (CCSN) explosions are linked with the death of massive stars. However, because precise measurements of CCSN progenitor masses are scarce, the mapping between explosion scenario and the progenitor mass distribution is less clear. The most common method of progenitor mass determination is direct imaging, in which one identifies the progenitor star in multi-band pre-explosion imaging, fits a spectral energy distribution to the photometry, and verifies the star is gone once the SN has faded. This methodology is ideal given appropriate data, but it is limited to contemporary SNe that have pre-explosion Hubble Space Telescope (HST) or deep ground-based imaging. As a result, only  $\sim 25$  SNe have any constraint on their progenitor masses, and half of these are only upper limits (Smartt et al. 2002; Van Dyk et al. 2003a,b; Smartt et al. 2004; Maund et al. 2005; Hendry et al. 2006; Li et al. 2005, 2006, 2007; Smartt et al. 2009; Smartt 2009; Gal-Yam et al. 2007; Gal-Yam & Leonard 2009; Smith et al. 2011b; Maund et al. 2011; Van Dyk et al. 2011; Fraser et al. 2012; Van Dyk et al. 2012a,b). A significant increase

in the number of progenitor masses could allow us a powerful window into further understanding supernovae.

Direct imaging has created a prototypical picture of massive star death. Type II-P SNe are assumed to be created by red supergiant (RSG) stars with intact hydrogen envelopes, while more exotic SNe may be created by higher mass stars. However, a number of questions remain to be answered regarding supernova physics. Smartt et al. (2009) identify what they term to be the ‘red supergiant problem,’ an observed lack of progenitors of  $M_{\text{ZAMS}} \sim 16\text{--}30 M_\odot$  that we would expect to explode as Type II-P SN. A variety of channels have been proposed to account for these missing explosions, including direct black hole formation or the stars exploding as different SN types. Binarity of the progenitor system can also play a significant role in SN explosions. Smith et al. (2011a) show that numbers of Type Ibc and IIb explosions are significantly underestimated if single-star explosions are assumed to be the only SN channel.

These issues are difficult to address without further progenitors to analyze. Unfortunately, while direct-imaging of the progenitor star would be ideal, there are constraints that limit the frequency with which it may be applied. First, direct imaging is limited by the SN rate: roughly one per century in a large spiral galaxy (Cappellaro et al. 1999). Second, direct imaging requires that the host galaxy be close enough to resolve the progenitor star, an effective limit of  $\sim 20$  Mpc (Smartt 2009). Third, preexisting sub-arcsecond images of the site must exist, necessitating archival HST images with either the

<sup>1</sup> Box 351580, The University of Washington Seattle, WA 98195; zachjenn@uw.edu

<sup>2</sup> Department of Astrophysical Sciences, Princeton University, Princeton, NJ 08544

<sup>3</sup> Raytheon, 1151 E. Hermans Road, Tucson, AZ 85706; adolphin@raytheon.com

<sup>4</sup> Hubble Fellow

Wide Field Planetary Camera 2 (WFPC-2) or the Advanced Camera for Surveys (ACS). Finally, even with the existence of appropriate images, there is no guarantee that the precursor will be identified. For example, Smartt et al. (2009) summarized 20 progenitor detections in Type II-P explosions. Only five progenitors were directly observed, and an additional two which fell on compact star clusters were well constrained. The remainder had no detection, but were given upper bounds based on the maximum luminosity with which they could escape detection (see also Smartt et al. (2003); Van Dyk et al. (2003c); Maund & Smartt (2005)).

In short, while direct imaging is ideal given appropriate data, it suffers from prerequisites that limit the number of opportunities in which it may be applied. It is clear that development of an independent and complementary technique would be of interest.

In this paper we make use of an alternative technique, stellar population analysis, to infer progenitor masses. The technique involves examining a color-magnitude diagram (CMD) of the surrounding population of stars to infer an age and mass for the progenitor star. The advantage of our methodology is that we are not reliant on individual identification and photometry of the specific progenitor star, leaving us free to apply our method to cataloged supernova remnants (SNRs) in addition to directly observed SNe. This ability drastically increases the number of progenitor masses we may find, allowing us to make a more complete measurement of the underlying distribution of progenitor masses. Our method offers no direct way to probe the binarity of the system, which is relevant given the role binarity likely plays in certain CCSN scenarios. However, our estimate of the age of the surrounding stellar population is not affected by the particular details of a given progenitor system. Our method also offers no way to determine the type of CCSN explosion we are observing, so for SNR analysis we are not able to provide a direct link between SN explosion type and progenitor mass. However, we will be able to comment on the ranges of ZAMS masses that are producing CCSN explosions.

Stellar population analysis has been used many times historically to analyze the characteristics of progenitors. Many groups have carried out age dating of stellar clusters coincident with supernovae and derived corresponding stellar masses (Efremov 1991; Walborn et al. 1993; Panagia et al. 2000; Barth et al. 1996; Van Dyk et al. 1999; Maíz-Apellániz et al. 2004; Wang et al. 2005; Vinkó et al. 2009; Crockett et al. 2008). Badenes et al. (2009) examined the SFH map of the LMC published by Harris & Zaritsky (2009). They estimate ages and masses for the four most recent SNR produced by CCSNe in the LMC. In Gogarten et al. (2009a), we employed a technique identical to the one used in this paper to estimate the age of the progenitor of NGC 300 OT2008-1. We found that the star was likely to have formed 8-13 Myr ago, corresponding to a  $M_{\text{ZAMS}}$  of 12-17  $M_{\odot}$ . Finally, in Murphy et al. (2011) we applied the same technique as this paper to archival images of SN 2011dh, finding a most likely age of  $17^{+3}_{-4}$  Myr and a  $M_{\text{ZAMS}}$  of  $13^{+2}_{-1} M_{\odot}$ . Clearly there is a long list of successful applications of stellar population analysis leading to constraints on progenitor physical properties.

In this paper we examine 59 SNRs in the spiral galaxy M31, listed in Table 1. In §2 we outline the methods used to determine star formation histories (SFHs), ages, and masses for the progenitor stars. In §3 we present the results of the analysis. We find that 53 SNR display recent star formation, and we derive masses for these. We also present four example cases that are representative of the overall sample. Finally, in §4 we examine the distribution of progenitor masses. We search for indications of a minimum mass, which we find to be between 7.0 and 7.8  $M_{\odot}$ , and note that the distribution is more bottom-heavy than a Salpeter IMF distribution.

## 2. METHODOLOGY

The basic procedure for deriving a mass estimate for each progenitor is as follows. We first use coordinates from three SNR catalogs as explained in §2.2, which we assume are accurate to within a few arcseconds and unbiased to any one type of SN. We then search for any appropriate HST fields that contain the SNR in question. We perform photometry on the stars in each field, and create CMDs of the region within  $\sim 50$  pc of the SNR coordinates, assuming a distance modulus of  $m - M = 24.47$  (Stanek & Garnavich 1998). We use CMD fitting to measure the SFH of each region. For each region that displays recent SF, we use the age of this recent SF to associate an age with the progenitor star. Finally, we apply stellar evolution models to convert the age of the progenitor to the  $M_{\text{ZAMS}}$  of the progenitor.

### 2.1. Key Assumptions

Our method requires several assumptions to produce results. Above all, we must assume that some of the stars surrounding the SNR are in fact coeval with the progenitor star. There are several pieces of evidence suggesting this assumption is reasonable. First, 90% of stars form in clusters with sizes of  $\sim 1$  pc (Lada & Lada 2003). These stars are expected to stay spatially associated for timescales greater than the lifetimes of CCSNe progenitors, even for dissolving, unbound clusters. Second, theoretical predictions are that stars will stay spatially associated on scales of  $\sim 100$  pc for 100 Myr (Bastian & Goodwin 2006). Observational constraints support this (Gogarten et al. 2009b), as do simulations by Eldridge et al. (2011) who found that  $\sim 85\%$  of CCSNe will explode within 100 pc of their birth site. In addition, even if a progenitor would travel farther, we would still expect to see a fraction of the coeval young stellar population which is sufficient for age dating. The precise number of interest is the fraction of young stars that will stay within a certain distance in the lifetime of a core collapse supernova progenitor. The question is a complex one, and we know of no research that quantifies it precisely at this time. We conclude that it is a reasonable assumption that most of the young stellar population around our observed SNRs is coeval with their progenitors. Based on the analysis in Gogarten et al. (2009a), we adopt a value of  $\sim 50$  pc for the radius of our star selection annulus.

Our method does not assume any information about the type of SN that exploded. We assume that SNRs associated with recent star formation are CCSNe, but do not distinguish individual subtypes. For CCSNe, the particular type of supernova has no effect on our mass

determination process. However, the progenitors of thermonuclear Type Ia SNe are likely to arise from older stellar populations which may vary considerably more in age than the coeval populations of massive stars. While there exists considerable discussion in the literature as to the precise nature of Type Ia progenitor systems and their distribution in age (see Maoz & Mannucci (2012) and references therein), we would expect to see Type Ia progenitors ranging from ages of a few hundred Myr to several Gyr. Since these timescales are comparable to or significantly greater than the dynamical timescale of M31, our methodology of identifying and analyzing coeval stars is ineffective at measuring the precise ages of Type Ia progenitors.

Our method does have the risk of misinterpreting a Type Ia SNR as a CCSNR. In their volume limited sample ( $D < 60$  Mpc), Li et al. (2011) find that Type Ia SN compose 24% of observed SN. However, there are several qualitative reasons as to why one would expect a smaller Ia/CCSN fraction in our survey.

First, there is some discussion as to whether such a volume-limited survey may underestimate the fraction of CCSN due to their faintness compared to Type Ia SN (see discussions in Thompson et al. (2009); Horiuchi et al. (2009); Horiuchi et al. (2011)). This potential bias suggests that 24% could be considered an upper limit. In addition, the areas of M31 with greater HST coverage are primarily star forming regions, where we would naively expect CCSN to be more common, increasing the relative fraction of CCSN. Thus the actual fraction of Type Ia SNR we expect in our sample is probably somewhat less than 24%.

Moreover, it is likely that some Type Ia SNR can be identified by their lack of an associated young stellar population. Badenes et al. (2009) examined four Ia sites in the LMC and found that three displayed a significant lack of recent star formation. Out of the 59 examined, we found 6 SNR displayed no recent SF in their surrounding stellar populations.

Finally, we have examined what effect additional hidden Ia contamination will have on our data. The procedure we used is explained in §4.3. We found that additional Ia contamination up to a total fraction of  $\sim 25\%$  has very little effect on the overall distribution observed in the sample.

To summarize, we argue that there are several qualitative reasons to assume that the effective Ia fraction in our sample is smaller than 24%. In addition, our method offers a means to identify and remove some SNR that are likely Ia progenitors. Finally, our overall results are largely insensitive to inclusion of additional Ia contamination up to the 24% observed in the volume-limited survey from Li et al. (2011).

Another possibility for SNRs with no coincident young SF is that they are the result of high-velocity progenitor stars that have left their birth sites. As a test of this possibility, we examined any site with no observed recent SF in GALEX FUV data. We found that all 6 sites with no recent SF are still relatively close ( $\sim 50$  to  $100$  pc) to GALEX FUV sources. If we assume that the progenitor star resulted from the most nearby FUV source for each zero-SF SNR, then a 50 Myr old star would only require velocities of a few km/s to reach the SNR site from the FUV source site, well within reasonable velocities for

runaway stars. Higher mass stars would of course require higher velocities to leave the FUV source in their shorter lifetimes. This analysis suggests that our study is unable to differentiate between Type Ia SNR and SNR resulting from high-velocity stars. We note, however, that a null-result for progenitor mass will not affect the distribution of progenitor masses we measure. It will simply reduce our effective sample size.

Finally, our method is highly contingent on the accuracy of the stellar evolution models used to model our observed CMDs. Because the models are theoretical, they generally do not have easily quantifiable uncertainties. The wide array of available model sets tend to systematically differ in bolometric luminosity and temperature, but are consistent within about 0.2 mag in bolometric luminosity and 0.02 dex in log temperature. We therefore quantify the uncertainty of our results due to the models used by including random shifts in the bolometric luminosity and temperature of the models as part of our Monte Carlo (MC) tests (see also Dolphin (2002)). We detail the process further in §2.5.

## 2.2. Data and Photometry

There are only a few extensive catalogs of SNRs in M31. We use the catalogs of Braun & Walterbos (1993), Magnier et al. (1995), and Williams et al. (1995). All three make identifications based on [SII]-to- $H\alpha$  ratios, and Magnier et al. (1995) make additional use of morphology and OB star associations. Magnier et al. (1995) identify three confidence levels based on approximate levels of contamination, although they note that the confidence levels are somewhat subjective. We only perform analysis on their first and second confidence candidates. The catalogs are not mutually exclusive, and the coverage areas of the three catalogs overlap in several areas, causing several remnants to be identified in both catalogs. To avoid treating a double-identified remnant as two separate remnants, we identify all remnants from two separate catalogs in which the 50 pc areas overlap and only select coordinates from one catalog. In these duplicate cases, we adopted the coordinates first from Braun & Walterbos (1993), then from Magnier et al. (1995) if Braun & Walterbos (1993) did not identify a remnant in that position. On occasion, a single catalog identified two remnants in which these 50 pc regions overlapped, but we still performed analysis on both candidates in such a case. In addition, we cross-referenced the SNR catalogs with Sasaki et al. (2012) and eliminated two, K567 and K884, which were found to not be SNR based on their optical/X-ray properties.

For our analysis, we require that the stellar population surrounding the SNR be imaged by either the Advanced Camera for Surveys (ACS) or the Wide-Field Planetary Camera 2 (WFPC2) instruments on HST in at least two broadband filters. We also require our 50% completeness limits (see §2.3) for a given CMD to be at least 24.5 magnitude in F475W, F555W, or F606W, whichever represents the blue filter (all qualifying fields of sufficient depth were either F475W, F555W, or F606W vs. F814W). The location of the MS turnoff is very similar in color in these filter sets, so adopting a similar magnitude cut in all three is reasonable.

Our comparisons between SNRs imaged multiple times at varying depths indicate that simply reaching the MS

turnoff for a given CMD is insufficient to correctly determine the age. CMD fitting is highly sensitive to densities of stars at given ages, requiring a well-sampled stellar population at the age of interest. In general, we found that our methodology applied to shallower data had a tendency to miss older bursts of SF which still may have resulted in CCSN. The available 2-filter broadband data for M31 happens to be distributed in two groups, including many shallow fields (blue depth < 23) and many deep fields (blue depth > 25), with very few in between. The choice of our depth cut causes us to reject five SNR that have only been imaged with shallow WFPC-2 data.

In Table 1 we list the SNR for which our criteria is met, along with the corresponding HST fields. In cases where the regions in question were imaged multiple times, we selected whichever set of images had the greatest number of stellar detections. In Fig. 1 we chart the locations of the examined remnants on a star-subtracted image of M31 in  $H\alpha$ . Those remnants colored red represent probable Ia candidates, where no young SF was found. There is a clear grouping of CCSN candidates along the star forming arms of M31.

We performed resolved stellar photometry using the photometry pipeline developed for the ACS Nearby Galaxy Treasury program (Dalcanton et al. 2009). This pipeline uses the DOLPHOT stellar photometry package (Dolphin 2000) to fit the well-characterized ACS point spread function to all of the point sources in the images. We then converted fluxes to Vega magnitudes using the standard zero-points and aperture corrections from the ACS handbook. We assess photometric errors and completeness using fake star tests. At least  $10^5$  tests are performed by inserting fake stars of known color and magnitude into the data one at a time and blindly attempting to recover them with the same software. Both fake star tests and photometry were performed on the full HST fields.

### 2.3. Calculation of Star Formation Histories

CMD fitting is a powerful tool for measuring star formation histories (Gallart et al. 2005; Barker et al. 2007; Williams et al. 2009a,b; Tolstoy et al. 2009). To estimate star formation histories of the regions surrounding the SNR, we used the software package MATCH (Dolphin 2002). MATCH works by creating many model CMDs based on theoretical isochrones for a variety of ages and metallicities. A linear combination of these model CMDs are then fit to the observed CMD. We use the models of Marigo et al. (2008) and Girardi et al. (2010) both for CMD fitting and estimation of  $M_{ZAMS}$ .

For each field, we selected stars from our photometry catalog within a  $15''$  radius around the SNR coordinates, which equates to a physical size of  $\sim 50$  pc at an assumed distance modulus of  $m - M = 24.47$  (Stanek & Garnavich 1998). This is consistent with the spatial correlation discussed in §2.1. We account for photometric errors through the use of fake star tests. We selected fake stars in a region  $\sim 2.5$  times the radius of the real star annulus to ensure that at least a few thousand recovered fake stars are included for each SNR. We defined lower magnitude limits as the point at which fake star completeness dipped below 50%.

MATCH requires a variety of parameters to generate and fit CMDs. We assumed a Salpeter IMF,  $dN/dM =$

$M^{-2.35}$  (Salpeter 1955), and a binary fraction of 0.35. Gogarten et al. (2009a) demonstrated that varying the IMF value from -2.0 to -2.7 or varying the binary fraction from 0.2 to 0.5 had no effect on the epoch assigned to a recent burst. We also varied the IMF from -1.3 to -3.3 for select regions and found no significant difference in relative fractions of SF for various epochs. Although absolute amplitudes of SF did change, only relative amplitudes have an effect on our method of determining ages. Note that the IMF and binary fraction are used by MATCH purely for purposes of populating the models. We assume nothing about either value with regards to a potential CCSN progenitor system or the overall progenitor mass distribution.

MATCH produces fits in logarithmic age bins. We adopted 71 age bins increasing in .05 increments from 6.60 (4 Myr) up to 10.10 (12.5 Gyr). We are unable to fit for ages younger than this due to the lack of isochrones at younger ages. MATCH will interpret any SF from a population younger than the 6.60 to 6.65 (4 to 4.5 Myr) bin as being included in this bin. Thus our youngest bin actually includes all SF from present times back to 4.5 Myr. As a result, we may only quote an upper age limit for any SF found in this youngest bin. In Fig. 2 we plot the isochrones for every-other age bin from 6.60 through 8.00 in F555W vs. F555W-F814W.

Fitting metallicity with MATCH is not viable given the very weak dependence of the optical colors of the upper main sequence on metallicity. We therefore constrained the metallicity to a spread of  $\sim 0.15$  dex and to increase with the lifetime of the galaxy, which consistently produced best-fit metallicities of solar. This value is consistent with the known gas-phase metallicity of M31 (Dennefeld & Kunth 1981; Blair et al. 1982). Finally, we binned our CMDs in units of 0.3 in magnitude and 0.15 in color. This binning accounted for the fact that some fields had few upper MS stars, allowing us to reduce the impact of this paucity on our fits. However, we still maintain a number of bins significantly larger than the number of free parameters used in the fitting. We experimented with using finer binning and found no change in our age determinations within our uncertainties.

### 2.4. Treatment of Reddening

Recent SFHs are very sensitive to the treatment of reddening. Our most simplistic treatment of reddening is to assume that all reddening is due to a galactic foreground, search over a specified range of reddening values for a best fit, and apply this value to the CMD as a whole. However, we frequently found significant differential reddening ( $dA_v$ ) across our small SNR-centered regions, which manifests as an increased width to the MS and red clump. Star forming regions will typically have extensive amounts of dust and gas, often not uniformly distributed, and as such there is no reason to believe that a single reddening value would correctly describe the region as a whole. MATCH by default allows for 0.5 mag of differential reddening for populations below 40 Myr, after which it falls linearly down to 0.0 mag at 100 Myr. In addition, the user has the ability to add additional full-field differential reddening across the CMD. We almost always found that the default treatment of reddening was inadequate to account for all the reddening present in the

regions.

As an example of how ignoring differential reddening can lead to an erroneous result, we consider the SNR BW-102. The photometry is quite deep, extending to magnitudes of  $F475W = 27.6$  and  $F814W = 26.8$ . In the left panel of Fig. 3 we plot the observed CMD of the region, as well as the best-fit model generated by MATCH in the background in greyscale. In the right panel, we plot the cumulative SFH as a fraction of total SFH in the past 50 Myr, assuming a fixed differential reddening of  $dA_v = 0.5$  mags affecting only the young stars. We found a best-fit reddening value of  $A_v = 0.975$ . All the star formation is concentrated in the youngest time bin ( $< 4.5$  Myr), corresponding to a lower limit  $M_{ZAMS}$  of  $52 M_\odot$ . However, several qualities of the CMD would cause us to be suspicious of this result. The main sequence appears very dim, and appears to contain lack the young, bright, blue stars that the model predicts at  $F475W < 22.5$ . We would not expect this given a result of very extensive young star formation. Looking beyond the main sequence, we see that the red clump is extended over nearly 2 magnitudes in  $F475W$ . Indeed, the model very poorly models the stars at  $F475W \sim 25.5$ ,  $F475W - F814W \sim 1.75$ . Thus not only was the default value of differential reddening insufficient to model the entire CMD, the treatment of differential reddening as something unique to the young stellar population is clearly not reflected in the reality of the CMD. For regions such as this, it is necessary to apply differential reddening across the CMD. We must then define the amount of differential reddening to add.

To understand our technique for determining the amount of  $dA_v$  to use, we must expand on the differential reddening model used by MATCH. MATCH applies differential reddening to the model CMDs by applying a top-hat distribution along the reddening line. The low end of the top-hat is defined by a foreground value of  $A_v$  for which MATCH fits. The width of the distribution is then defined by the specified value provided by the user. When applying additional differential reddening, fit values tended to improve until we reached unphysical values of  $dA_v$ . The only true constraint we may apply is that this minimum value of  $A_v$  must be at least equivalent to the Milky Way foreground value. Schlegel et al. (1998) find a foreground reddening value to M31 of  $A_v = 0.19$ . While this value is likely to change slightly over the angular size of M31, the changes will clearly be small compared to the magnitude of differential reddening internal to M31. Our solution to CMDs such as BW-102 is to increase the width of the differential reddening distribution applied to all ages until the best-fit value of  $A_v$  MATCH finds reaches the foreground value. We then use this differential reddening distribution to measure the SFH and derive the age of the SN progenitor.

In Fig. 4 we plot the SFH results for a variety of differential reddening values, increasing from  $dA_v = 0.0$  up to  $dA_v = 1.5$  magnitudes, in increments of 0.1. Note that this differential reddening is in addition to the default young  $dA_v = 0.5$ , leading to up to 2.0 magnitudes of differential reddening on the very youngest stellar populations. We found that a value of  $dA_v = 1.5$  was the point at which the overall reddening value dropped to the expected foreground value for BW-102. For this value of differential reddening, the SFH corresponded to an age

of 36 Myr and a mass of  $\sim 9 M_\odot$ , a much more reasonable result given the observed CMD. Note that the SFH reaches this result (within uncertainty) before the best-fit  $A_v$  value reaches foreground, suggesting that our result is not highly contingent on the precise value of foreground reddening assumed. In the left panel of Fig 5 we plot the observed CMD with the best-fit model plotted in greyscale in the background, created using the above  $dA_v$  procedure. In the right panel, we plot the cumulative SFH of the region for the past 50 Myr, with error bars from the Monte Carlo analysis described in §2.5

We found essentially all fields suffered from differential reddening in excess of the default values used by MATCH. When no extra differential reddening was included in the models, many regions without obvious young star formation were best fit by high overall reddening values and included star formation in the youngest few time bin. The issue arises from faint main sequence stars revealed by deep photometry. Without inclusion of differential reddening, these stars are fit by the uniform foreground reddening value for the region, which is typically a high value (e.g.  $A_v > 0.6$ ). Using this erroneously high value, the stars are corrected to be brighter and bluer than they actually are, leading MATCH to mistake them as evidence of young star formation. By allowing for differential reddening, we can incorporate the full range of different reddening values across the field.

For our final procedure, we increase the amount of full-CMD differential reddening until we find the best fit  $A_v$  reaches the foreground value,  $A_v = 0.19$ . We then adopt this value of differential reddening for subsequent analysis of that particular SNR.

## 2.5. Assessing Uncertainties

### 2.5.1. Multiple Coeval Populations

Our ultimate goal is to estimate the mass of the progenitor. We do this by identifying the burst of recent star formation from which the progenitor star most likely originated, allowing us to assign an age to each progenitor star. Ideally, each SFH would have a single isolated burst, making it easy to associate a single age to the young stellar population. In many cases, however, multiple bursts of varying rates and durations appear in the young star formation history. As a result, we examine the cumulative star formation history of each CMD as a fraction of the total recent star formation. When examined as such, the fraction of star formation in each age bin corresponds to the probability that the progenitor will be of that age. Because we are only interested in recent SF, we examine only the most recent 50 Myr of SF (see §4.1 for an explanation of this limit).

### 2.5.2. Fitting Errors

Our results suffer from both random uncertainties due to the sampling of the CMD and systematic errors due to differences between the theoretical isochrones and observations. For example, if the models were consistently redder than the observed stars, we would generally find younger ages when these models are applied to real data. The random errors are generally highly dependent on the number of upper main sequence stars in the field, with higher numbers providing a tighter constraint on the data (although more upper main sequence stars may also sim-

ply indicate a younger population). See Gogarten et al. (2009a) for further discussion of this point.

To analyze our uncertainties, we performed a series of Monte Carlo (MC) realizations of the data (see also Dolphin (2002); Weisz et al. (2011)). In each MC run, we re-sampled the observed CMD to account for the Poisson errors of the stars. In addition, to estimate how systematic model differences can impact the results, we add in random shifts to the models for each run. We used random shifts of  $\sigma = 0.02$  in temperature and  $\sigma = 0.17$  in bolometric luminosity. These systematic offsets are much larger than uncertainty in the distance modulus, thereby incorporating both effects into our overall uncertainty analysis.

Uncertainty in the age of the recent star formation manifests itself in two distinct ways. The first is uncertainty measured by the MC analysis performed above, while the second is due to the width of the intrinsic spread of the burst across multiple age bins. We estimate the latter of these as the difference between the median age and the ages where 16% and 84% of star formation has occurred. We estimate the former of these as the RMS difference between the median age of the best fit and the median ages of SF from the MC tests. We then add these differences in quadrature to assign a confidence interval to each result. Thus for each progenitor we determine a median age, as well as (potentially asymmetric) uncertainties about this median. Finally, we make the assumption that we are unable to determine the age of SF to a greater precision than the age bins in which we have measured this SF. We thus round the age range to the age of the next isochrone out from the median. We perform this step for both younger and older star formation, always rounding away from the median. The ages of these isochrones determine our final uncertainties.

In order to use this method of analysis, we must define the maximum age of star formation which may produce core-collapse progenitors. As explained in §4.1, we use our distribution to estimate a minimum mass for core-collapse between 7.8 and 7.0  $M_{\odot}$ . As a result, we adopt 50 Myr as the maximum age of a core-collapse progenitor and only perform the above mass estimation analysis over the most recent 50 Myr of SF.

### 2.6. Converting SFH to Progenitor Mass

The Marigo et al. (2008) and Girardi et al. (2010) models specify a maximum mass for an isochrone at a given age. More massive stars will have already died off. Thus the isochrones we have identified as bounding our confidence interval can be linked directly to values for  $M_{\text{ZAMS}}$ . Our value for the median progenitor mass comes from interpolating the final isochrone masses between isochrones to the median age value. This is necessary because our median age won't line up exactly with a defined isochrone.

In Fig. 6 we plot the Marigo et al. (2008) and Girardi et al. (2010) isochrones for final isochrone mass vs. age for metallicities of  $Z = 0.004, 0.008, 0.019,$  and  $0.030$ . The models produce very similar age to mass conversions regardless of the assumed metallicity. The vast majority of our regions produce best fit metallicities of approximately solar. As a result, we adopt the  $Z = 0.019$  isochrone for mass determinations. Note that masses change very quickly for younger populations,

while masses for older populations change at a much slower rate. This means that our results for less massive progenitors will naturally be more precise.

Note that we have neglected systematic uncertainties in the age-to-mass conversion process for our individual progenitor results. This leads to very small error bars on some progenitor masses, especially those at older ages, where mass doesn't change significantly as a function of age. Our mass distributions are not sensitive to this model-dependent systematic uncertainty, as shown by similarity between the median progenitor distribution and the probability distribution (see §4.2). However, uncertainties are almost certainly underestimated for some progenitors, especially at the low-mass end. To estimate the magnitude of this systematic uncertainty, we compared the solar metallicity isochrones of Pietrinferni et al. (2004) to the Marigo et al. (2008); Girardi et al. (2010) isochrones used for our analysis. We found that for a  $\sim 50$  Myr lifetime star, the Pietrinferni et al. (2004) isochrones find a maximum mass of 6.7  $M_{\odot}$ , compared to the 7.3  $M_{\odot}$  predicted for the Marigo et al. (2008); Girardi et al. (2010) isochrones. At a lifetime of  $\sim 22$  Myr, the youngest stars tested by Pietrinferni et al. (2004), the maximum masses for the different isochrone sets are 9.9  $M_{\odot}$  and 10.9  $M_{\odot}$  respectively. These suggest systematic uncertainties of around 0.5-1.0  $M_{\odot}$  for the age-mass conversion process. Again, we do not include these systematic uncertainties in the reported values in Table 2; the reader should keep this in mind when interpreting the results of any individual progenitor star in our study.

## 3. RESULTS

In Table 2 we list results for all 59 SNR analyzed. We tabulate the designation, mass, age, number of main sequence stars (defined as  $F475W - F814W \leq 0.4$ ,  $F555W - F814W \leq 0.4$ , and  $F606W - F814W \leq 0.3$ ), total stellar mass, and additional full-field  $dA_v$  applied. In general the number of MS stars may be taken as an indication of confidence in the answer, but older populations will also generally have fewer MS stars. As a result, this mapping is very approximate. The total stellar mass listed is highly dependent on the precise value selected for the IMF, and as such should not be taken as an exact measurement. It is intended only to compare relative amplitudes of star formation between various SNR regions. We observe six fields that have no significant recent SF, and identify these as likely either Type Ia SNR or SNR resulting from runaway progenitor stars. They are not included in analysis of the distribution of recovered progenitor masses.

To examine any underlying biases in our data selection, we plot the recovered ages against the 50% completeness magnitudes in Fig. 7. The top panel displays the bluer filter for each particular CMD, while the bottom is for the redder (F814W in all cases). Following application of our depth requirement, we find no evidence of any correlation between recovered age and depth of data.

The top panel of Fig. 8 plots the recovered ages as a function of the number of MS stars detected. The bottom panel plots recovered ages as a function of  $dA_v$  used. Note that these values only include full-field  $dA_v$ , not the 0.5 mag of  $dA_v$  included for all young populations. No correlation is observed in either comparison, which

suggests that our treatment of differential reddening from §2.4 does not bias us towards a specific age.

While an in-depth discussion of all SNR is prohibitively long, it is worth exploring a representative sample of the various cases observed. In general, fields with fewer main sequence stars will tend to have larger uncertainties, and we list our results in Table 2 in order of the number of these stars. However, this generalization is not absolute, and this ordering should be taken as approximate. Finally, some of the regions display no young star formation, which we list in a separate category. For illustrative purposes, we subjectively identify four classes of results. Below we examine four representative SNR for each case.

### 3.1. K376: Obvious Young Star Formation

In the left panel of Fig. 9 we display the color-magnitude diagram for the region around K376, plotted in red. We also plot our best-fit model CMD in the background in greyscale, with darker regions corresponding to a larger expected stellar density. The data we used for K376 are from HST project 12055 (Brick 9, Field 14), and included ACS images in F475W and F814W. The photometry is fairly deep, with 50% completeness limits at F475W=27.1 and F814W=25.8. We find 6874 stars in the 50 pc region around the SNR, 350 of which are MS stars, making K376 a very well populated CMD.

A qualitative inspection of the CMD indicates a bright, blue upper main sequence, indicative of a significant young stellar population. The CMD displays a great deal of differential reddening, as indicated by a large spread in the red clump. We used a full-field value of  $dA_v = 0.7$ , in addition to  $dA_v = 0.5$  for young stars, to model this CMD. MATCH predictably finds that this CMD displays significant young star formation: we find the field well fit by a single burst of star formation at  $12 \pm 1$  Myr, corresponding to a mass estimate of  $16 \pm 1 M_\odot$ . The older burst at  $\sim 40$  Myr is of significantly lower prominence compared to the young burst. The result is well-constrained due to the large number of stars in the field.

Similar SNR include 2-020, 2-024, K934, K947, BW-60, BW-69, BW-74.

### 3.2. K180: Well Defined Older Populations

Fig. 10 displays the CMD and SFH for the region surrounding K180. The data for K180 are from HST project 12073 (Brick 2, Field 11), and includes ACS images in F475W and F814W. The photometry is quite deep, with 50% completeness limits of F475W=27.2 and F814W=25.9 respectively. We find 3950 stars in the CMD, 162 of which are MS stars. We used full-field value of  $dA_v = 0.6$ , in addition to  $dA_v = 0.5$  for young stars, to model this CMD.

The upper main sequence is not nearly as bright or prominent as that of K376, and as such we would predict an older population with a lower mass progenitor star. MATCH agrees, finding the population is fit best by a single burst of star formation at  $33 \pm 2$  Myr, corresponding to a mass of  $8.8 \pm 0.2 M_\odot$ . As above, because of the large number of stars in the field, the mass is fairly well constrained.

Similar SNR include 1-006, 1-008, 1-009, 1-010, 2-025, 2-044, 2-046, 2-048, 2-050, K516, K526A, K574, K594, BW-18, BW-20, BW-31, BW-32, BW-76, BW-81, BW-84, BW-86, BW-102, and BW-110.

### 3.3. K891: SF Spread Over a Wide Range

Fig. 11 displays the CMD and SFH for the region surrounding K891. The data for K891 are from HST project 12055, including ACS images in F475W and F814W. The photometry is again quite deep, with 50% completeness limits of F475W=27.6 and F814W=26.6 respectively. The CMD has 1441 total stars, including 149 MS stars. We used a full-field value of  $dA_v = 1.1$ , in addition to  $dA_v = 0.5$  for young stars, to model this CMD.

The CMD for K891 doesn't appear to comprise a single uniform population, and indeed has stars spread out at a wide variety of ages. MATCH finds two distinct star formation bursts: one in our youngest age bin at less than 4.4 Myr, and another in an older bin at  $\sim 32$  Myr. The error bars also indicate that the relative prominence of these bursts is such that we may not favor one burst over the other. While we find a median mass of  $\sim 9 M_\odot$ , the uncertainties allow this result to range over all almost masses past the minimum mass for core-collapse. K891 is an example of a SNR where we have reasonable confidence in our answer, but this answer allows no constraint on the parameters we ultimately wish to measure.

Similar SNR include 2-049, K446, K497, K525A, K527A, K856A, K908, K956A, BW-11, BW-39, BW-44, BW-61, BW-65, BW-66, BW-71, BW-77, BW-82, BW-89, BW-105, and BW-106.

### 3.4. 2-028: No Recent Star Formation

Fig. 12 displays the CMD and SFH for the region surrounding 2-028. The data for 2-028 is also from HST project 10273, and includes ACS images in F555W and F814W. The photometry has more shallow 50% limits than the CMDs above, with F555W=25.7 and F814W=25.4 respectively. The CMD has only 374 stars, a smaller number of detections than typical, including 53 MS stars. We used a full-field value of  $dA_v = 0.5$ , in addition to  $dA_v = 0.5$  for young stars, to model this CMD.

The CMD clearly has a very sparse and dim main sequence, leading us to predict that MATCH would find little to no young star formation. Indeed, MATCH finds the youngest star formation as occurring at older than 90 Myr, well beyond the age of stellar populations that we would expect to produce progenitors of core-collapse SNe. We classify this SNR as the result of either a Type Ia SN or a runaway star that has left the young stellar population at its birth site. We do not use any results in this category as for purposes of analyzing the mass distribution.

Similar SNR include 2-016, 2-021, 2-026, BW-19, and BW-36.

## 4. DISCUSSION AND SUMMARY

### 4.1. Indications of a Minimum Mass

Our method measures the prominence of a burst as a fraction of the total recent SF. This approach requires that we define the period of time that we consider as "recent" SF. Specifically, we must identify the age range where star formation can produce stars massive enough to result in CCSNe. Theoretical arguments and observational evidence point to a minimum mass necessary for progenitors to undergo core-collapse to a neutron star. Stars below this mass are generally assumed to

leave behind white dwarf stars, producing no SN explosion. Thus one may constrain this cross-over mass by either measuring the maximum mass from which a star may create a white dwarf, or the minimum mass necessary for a star to explode. Measurements of white dwarfs have defined a lower limit on this minimum mass of 6.3-7.1  $M_{\odot}$  (Williams et al. 2009c), corresponding to an age of between  $\sim 55$  and 63 Myr, and direct progenitor mass measurements has converged on a value of  $8 \pm 1 M_{\odot}$  (Smartt et al. 2009; Botticella et al. 2012), corresponding to an age of between  $\sim 33$  and 55 Myr.

In our observed progenitor mass distribution, we would expect to see the following behavior: above the minimum mass for core-collapse, we expect the distribution of progenitor masses to follow the IMF, assuming that the recent SFR is approximately constant. Below the minimum mass, the inferred progenitor mass should have no physical connection to the CCSNe process and should reflect random sampling of the SFR at  $>50$  Myr, producing an essentially flat distribution in inferred progenitor mass.

In the left panel of Fig. 13, we plot the distribution of progenitor masses for a variety of assumed minimum masses. We vary the minimum mass from 9.6  $M_{\odot}$  to 6.0  $M_{\odot}$  (our chosen masses are mapped using the  $M_{\text{ZAMS}}$  from Marigo et al. (2008) and Girardi et al. (2010) isochrones). We find that for assumed minimum mass greater than 8.1  $M_{\odot}$ , the distribution increases until the assumed minimum mass is reached. For assumed minimum mass values below 8.1  $M_{\odot}$ , there is a peak between 7.5 and 8.5  $M_{\odot}$ , below which the number of progenitors drops, suggesting a minimum mass in this range.

To find the actual minimum mass, we lower the assumed minimum mass until the measured minimum mass no longer reflects this assumed value. We note the amplitude of the peak in the distribution is greatest for an assumed minimum of 7.3  $M_{\odot}$ . To quantify the location of this peak, we calculate the derivative of the number of progenitors as a function of mass. We assume that the maximum value of this derivative occurs at the minimum mass a star undergoes core-collapse, as this value identifies the beginning of the peak. In the right panel of Fig. 13 we plot the location of this maximum against our assumed minimum mass. We note that above an assumed minimum mass of 7.3  $M_{\odot}$ , the peak value traces the assumed minimum mass. For 7.3  $M_{\odot}$  and below, however, the peak value is always around  $\sim 7.5 M_{\odot}$ . If we assume our uncertainties are at least the width of the mass bins, then we find a minimum mass for core-collapse between 7.0 and 7.8  $M_{\odot}$ . This range is consistent with the observational measurements of Smartt et al. (2009) and Botticella et al. (2012). We therefore have adopted the 44.7 to 50 Myr (7.7 to 7.3  $M_{\odot}$ ) bin as the oldest included for our final results.

#### 4.2. Progenitor Mass Distribution

In the left panel of Fig. 14 we plot the histogram of median progenitor masses, restricted to 7  $M_{\odot}$  and above. In the right panel of Fig. 14 we plot the cumulative fraction of progenitor masses. Unless otherwise noted, we assume a maximum mass of 120  $M_{\odot}$ , although the choice of this value at high masses is essentially irrelevant to the overall distributions given the rarity of extremely massive stars.

Qualitatively, the observed distribution shows a lack of the most massive stars when compared to a Salpeter IMF ( $dN/dM \propto M^{\alpha}$ , where  $\alpha = -2.35$ ). We performed a Kolmogorov-Smirnov (KS) test, assuming a single power law distribution. We found values of  $\alpha$  outside the range  $-2.7 \geq \alpha \geq -4.4$  inconsistent with the measured distribution at 95% confidence. Alternatively, we may consider a model distribution that is a Salpeter IMF ( $\alpha = -2.35$ ) up to some maximum mass, which we may vary. We found that this model was inconsistent with the data at 95% confidence at assumed maximum masses  $> 26 M_{\odot}$ . However, precise determination of this value is difficult in our survey due to the intrinsic rarity of massive stars and the mass spacing in our isochrones (see Fig. 6). Rather, this value represents the sort of mass range in which one must consider CCSN possible in order to maintain a Salpeter IMF.

In either scenario, the full distribution of measured masses suggests that some fraction of massive stars are not exploding as CCSN. This result has interesting implications for CCSN physics. A wide variety of SN channels have been explored both theoretically and observationally in the literature. Theoretical predictions have explored the possibility of direct black hole formation beyond a certain mass threshold somewhere around  $\sim 25 M_{\odot}$ . The manifestation of such events in an overall mass distribution would be an observed lack of progenitors beyond the mass threshold, essentially a more bottom-heavy IMF than that of all massive stars. While the reality is likely something more complicated than a well-defined threshold between CCSN and black hole formation (many different scenarios likely combine to produce a complicated mass distribution), the qualitative effect will be that which we observe in our distribution.

Smartt et al. (2009) first identified the red supergiant problem, an observed lack of Type IIP progenitors between 16 and 30  $M_{\odot}$ . Many solutions have been proposed to explain the problem (see Walmswell & Eldridge (2012) and references therein). In addition, the recent SN 2012aw may fall in this mass range (Fraser et al. 2012; Van Dyk et al. 2012a), suggesting the possibility that Type IIP progenitors do exist in this range and have simply not yet been observed in sufficient number. We identify six progenitors with median progenitor masses between 16 and 30  $M_{\odot}$ , although the uncertainties on many of these are large. If our progenitors were sampled uniformly from a Salpeter IMF, we would expect to find  $\sim 10$  progenitors (20%) in the mass range from 16 to 30  $M_{\odot}$ . Thus while we don't observe a complete lack of progenitors in the specified mass range, we do observe fewer than we would expect given a Salpeter IMF distribution.

Finally, while we assumed our SNR catalogs constituted a complete, unbiased sample, the possibility exists that selection effects in the catalogs lead to the lower end of the progenitor mass distribution being sampled more heavily. In particular, extremely massive progenitors are likely associated with strong H II regions, where identification of SNRs is a more difficult observational task. It is possible SNRs of this type are systematically undersampled in the survey.

We attempted to quantify both the IMF slope and minimum mass using Markov Chain Monte Carlo methods, but found that the data could not produce meaningful



constraints beyond those determined by our more simplistic techniques. We believe the chief reason for this is the size of errors due to differential reddening of the fields. Part of the problem is treatment of differential reddening as a top-hat distribution. In addition, the inclination of M31 contributes to these high differential extinction values. The application of this technique to a less inclined galaxy would be of benefit in this respect. Finally, the simple addition of more progenitor mass estimates would allow us to better constrain our analysis. We are currently performing identical analysis on an additional  $\sim 65$  SNR in M33 in pursuit of these final two points.

#### 4.3. Type Ia Contamination

Type Ia SNRs coincident with star-forming regions could in principle affect our mass distribution. To test the possibility of additional Type Ia contamination beyond the 11% observed, we examined Galex FUV fluxes at the sites of all SNR in our sample. We assumed that sites with the lowest FUV flux corresponded to possible older Type Ia sites which happened to be coincident with a small amount of recent SF. The eight lowest flux SNR (not including the 6 with no recent SF) were BW-18, BW-69, 1-006, 1-010, 2-024, 2-050, K891, and K956a. From Table 2, these additional SNRs in general have fewer MS stars and less total SF than most SNRs in the sample. We found that after removing these SNR, our observed distribution now ranged from  $-2.6 \geq \alpha \geq -4.3$ , which is consistent with our earlier measurement. This suggests that additional Type Ia contamination has little effect on our overall result, and still results in an IMF that is steeper than Salpeter (-2.35).

#### 4.4. Summary

Using resolved HST photometry, we have analyzed the stars surrounding 59 SNR in M31. Using CMD fitting, we calculate a SFH within a 50 pc radius of each SNR. We find that 53 of the SNR regions display significant evidence of recent star formation, which we use to age-date the progenitor star. The remaining six regions display no recent star formation, and we consider them either possible Type Ia candidates or the result of massive runaway progenitor stars.

We examine the distribution of progenitor masses for our CCSN candidates and find a lack of massive stars compared to a standard Salpeter IMF ( $dN/dM \propto M^\alpha$ , where  $\alpha = -2.35$ ). If a uniform single IMF is assumed, we find values for  $\alpha$  outside the range  $-2.7 \geq \alpha \geq -4.4$  inconsistent with the measured distribution at 95% confidence. Alternatively, if we consider a distribution that is a Salpeter IMF up to some maximum mass, we place an upper limit on the maximum mass allowed at  $M_{Max} \sim 26 M_\odot$ . We also estimate a minimum mass for core collapse of between 7.0 and 7.8  $M_\odot$ , which is both greater than the maximum mass for white dwarf collapse (Williams et al. 2009c) and consistent with direct progenitor measurements (Smartt et al. 2009; Botticella et al. 2012).

Z.G.J. is supported in part by funding from the Mary Gates Endowment. Z.G.J., B.F.W., and J.J.D. are supported in part by GO-12055. J.W.M. is supported in

part by an NSF Astronomy and Astrophysics Postdoctoral Fellowship under award AST-0802315. This work is based on observations made with the NASA/ESA Hubble Space Telescope, obtained from the data archive at the Space Telescope Science Institute. Support for this work was provided by NASA through Hubble Fellowship grant 51273.01 awarded to K.M.G. by the Space Telescope Science Institute. STScI is operated by the Association of Universities for Research in Astronomy, Inc. under NASA contract NAS 5-26555.

#### REFERENCES

- Badenes, C., Harris, J., Zaritsky, D., & Prieto, J. L. 2009, ApJ, 700, 727
- Barker, M. K., Sarajedini, A., Geisler, D., Harding, P., & Schommer, R. 2007, AJ, 133, 1138
- Barth, A. J., van Dyk, S. D., Filippenko, A. V., Leibundgut, B., & Richmond, M. W. 1996, AJ, 111, 2047
- Bastian, N., & Goodwin, S. P. 2006, MNRAS, 369, L9
- Blair, W. P., Kirshner, R. P., & Chevalier, R. A. 1982, ApJ, 254, 50
- Botticella, M. T., Smartt, S. J., Kennicutt, et al. 2012, A&A, 537, A132
- Braun, R., & Walterbos, R. A. M. 1993, A&AS, 98, 327
- Cappellaro, E., Evans, R., & Turatto, M. 1999, A&A, 351, 459
- Crockett, R. M., Eldridge, J. J., Smartt, S. J., et al. 2008, MNRAS, 391, L5
- Dalcanton, J. J., Williams, B. F., Seth, A. C., et al. 2009, ApJS, 183, 67
- Dennefeld, M., & Kunth, D. 1981, AJ, 86, 989
- Dolphin, A. E. 2000, PASP, 112, 1383
- 2002, MNRAS, 332, 91
- Efremov, Y. N. 1991, Soviet Astronomy Letters, 17, 173
- Eldridge, J. J., Langer, N., & Tout, C. A. 2011, MNRAS, 414, 3501
- Fraser, M., Maund, J. R., Smartt, S. J., et al. 2012, arXiv:1204.1523, Submitted to ApJL
- Gal-Yam, A., & Leonard, D. C. 2009, Nature, 458, 865
- Gal-Yam, A., Leonard, D. C., Fox, D. B., et al. 2007, ApJ, 656, 372
- Gallart, C., Zoccali, M., & Aparicio, A. 2005, ARA&A, 43, 387
- Girardi, L., Williams, B. F., Gilbert, K. M., et al. 2010, ApJ, 724, 1030
- Gogarten, S. M., Dalcanton, J. J., Murphy, J. W., et al. 2009a, ApJ, 703, 300
- Gogarten, S. M., Dalcanton, J. J., Williams, B. F., et al. 2009b, ApJ, 691, 115
- Harris, J., & Zaritsky, D. 2009, AJ, 138, 1243
- Hendry, M. A., Smartt, S. J., Crockett, R. M., et al. 2006, MNRAS, 369, 1303
- Horiuchi, S., Beacom, J. F., & Dwek, E. 2009, Phys. Rev. D, 79, 083013
- Horiuchi, S., Beacom, J. F., Kochanek, C. S., et al. 2011, ApJ, 738, 154
- Lada, C. J., & Lada, E. A. 2003, ARA&A, 41, 57
- Li, W., Leaman, J., Chornock, R., et al. 2011, MNRAS, 412, 1441
- Li, W., Van Dyk, S. D., Filippenko, A. V., & Cuillandre, J. 2005, PASP, 117, 121
- Li, W., Van Dyk, S. D., Filippenko, A. V., et al. 2006, ApJ, 641, 1060
- Li, W., Wang, X., Van Dyk, S. D., et al. 2007, ApJ, 661, 1013
- Magnier, E. A., Prins, S., van Paradijs, J., et al. 1995, A&AS, 114, 215
- Maíz-Apellániz, J., Bond, H. E., Siegel, M. H., et al. 2004, ApJ, 615, L113
- Maoz, D., & Mannucci, F. 2012, PASA, 29, 447
- Marigo, P., Girardi, L., Bressan, A., et al. 2008, A&A, 482, 883
- Maund, J. R., Fraser, M., Ergon, M., et al. 2011, ApJ, 739, L37
- Maund, J. R., & Smartt, S. J. 2005, MNRAS, 360, 288
- Maund, J. R., Smartt, S. J., & Danziger, I. J. 2005, MNRAS, 364, L33
- Murphy, J. W., Jennings, Z. G., Williams, B., Dalcanton, J. J., & Dolphin, A. E. 2011, ApJ, 742, L4

- Panagia, N., Romaniello, M., Scuderi, S., & Kirshner, R. P. 2000, *ApJ*, 539, 197
- Pietrinferni, A., Cassisi, S., Salaris, M., & Castelli, F. 2004, *ApJ*, 612, 168
- Salpeter, E. E. 1955, *ApJ*, 121, 161
- Sasaki, M., Pietsch, W., Haberl, F., et al. 2012, *A&A*, 544, 144
- Schlegel, D. J., Finkbeiner, D. P., & Davis, M. 1998, *ApJ*, 500, 525
- Smartt, S. J. 2009, *ARA&A*, 47, 63
- Smartt, S. J., Eldridge, J. J., Crockett, R. M., & Maund, J. R. 2009, *MNRAS*, 395, 1409
- Smartt, S. J., Maund, J. R., Gilmore, G. F., et al. 2003, *MNRAS*, 343, 735
- Smartt, S. J., Maund, J. R., Hendry, M. A., et al. 2004, *Science*, 303, 499
- Smartt, S. J., Vreeswijk, P. M., Ramirez-Ruiz, E., et al. 2002, *ApJ*, 572, L147
- Smith, N., Li, W., Filippenko, A. V., & Chornock, R. 2011a, *MNRAS*, 412, 1522
- Smith, N., Li, W., Miller, A. A., et al. 2011b, *ApJ*, 732, 63
- Stanek, K. Z., & Garnavich, P. M. 1998, *ApJ*, 503, L131+
- Thompson, T. A., Prieto, J. L., Stanek, K. Z., et al. 2009, *ApJ*, 705, 1364
- Tolstoy, E., Hill, V., & Tosi, M. 2009, *ARA&A*, 47, 371
- Van Dyk, S. D., Cenko, S. B., Poznanski, D., et al. 2012a, *ApJ*, 756, 131
- Van Dyk, S. D., Davidge, T. J., Elias-Rosa, N., et al. 2012b, *AJ*, 143, 19
- Van Dyk, S. D., Li, W., Cenko, S. B., et al. 2011, *ApJ*, 741, L28
- Van Dyk, S. D., Li, W., & Filippenko, A. V. 2003a, *PASP*, 115, 448
- 2003b, *PASP*, 115, 1289
- 2003c, *PASP*, 115, 1289
- Van Dyk, S. D., Peng, C. Y., Barth, A. J., & Filippenko, A. V. 1999, *AJ*, 118, 2331
- Vinkó, J., Sárneczky, K., Balog, Z., et al. 2009, *ApJ*, 695, 619
- Walborn, N. R., Phillips, M. M., Walker, A. R., & Elias, J. H. 1993, *PASP*, 105, 1240
- Walmswell, J. J., & Eldridge, J. J. 2012, *MNRAS*, 419, 2054
- Wang, X., Yang, Y., Zhang, T., et al. 2005, *ApJ*, 626, L89
- Weisz, D. R., Dalcanton, J. J., Williams, B. F., et al. 2011, *ApJ*, 739, 5
- Williams, B. F., Dalcanton, J. J., Dolphin, A. E., Holtzman, J., & Sarajedini, A. 2009a, *ApJ*, 695, L15
- Williams, B. F., Dalcanton, J. J., Seth, A. C., et al. 2009b, *AJ*, 137, 419
- Williams, B. F., Schmitt, M. D., & Winkler, P. F. 1995, in *Bulletin of the American Astronomical Society*, Vol. 27, American Astronomical Society Meeting Abstracts #186, 883+
- Williams, K. A., Bolte, M., & Koester, D. 2009c, *ApJ*, 693, 355

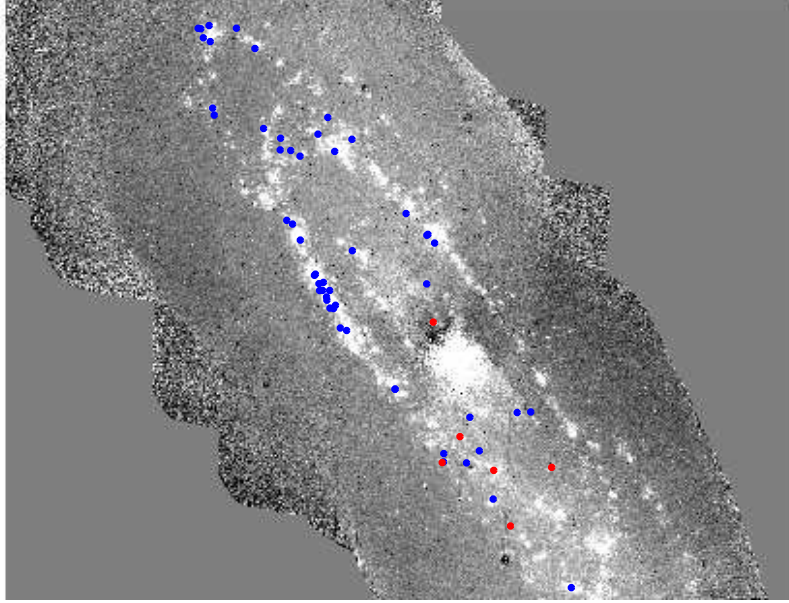


**Figure 1.** SN progenitor locations plotted on a star-subtracted  $H\alpha$  map of M31. SNRs in red correspond to those with no young SF detected. We consider these as possible Type Ia locations, or as the results of runaway stars. We note that a large amount of our CCSN candidates fall along the star forming arms of M31. This is clearly expected (CCSN candidates will tend to be found in regions of recent SF), but it also indicates the constraints imposed on our sample by the locations of archival HST data (star-forming regions are targeted significantly more than other areas).

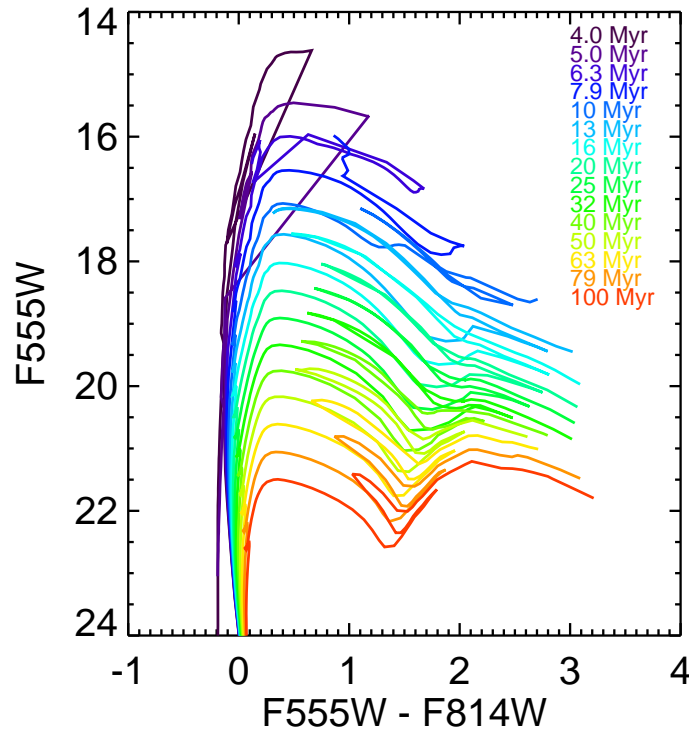


**Figure 2.** Marigo et al. (2008); Girardi et al. (2010) isochrones plotted in F555W against F555W - F814W for logarithmic age bins of 6.60 through 8.00. Redder isochrones correspond to older ages. We adopt the 50 Myr isochrone as the maximum age for a CCSN progenitor star, corresponding to a  $M_{ZAMS}$  of  $7.3 M_{\odot}$ . For clarity, we only plot every-other isochrone; our actual fitting procedure uses twice as many age bins over the same range.

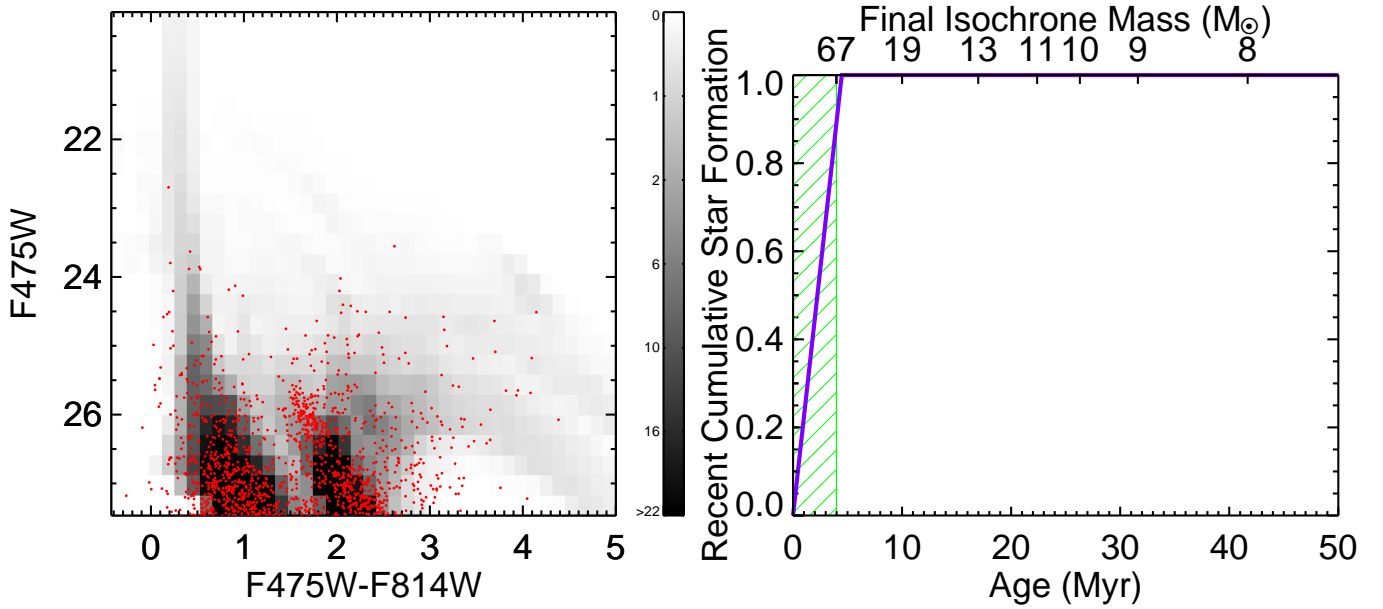


**Figure 3.** Left Panel: Observed CMD for the region around BW-102, F814W plotted against F475W-F814W. In the background we plot the best-fit model CMD generated by MATCH in greyscale, assuming no additional differential reddening. The model expects a much brighter MS than observed at  $F_{475W} < 22.5$  and poorly models the stars at  $F_{475W} \sim 25.5$ ,  $F_{475W} - F_{814W} \sim 1.75$  when differential reddening is not accounted for. Right panel: Cumulative recent star formation history calculated for the corresponding CMD. This SFH was from a blind run using MATCH's default values, with 0.5 magnitudes of differential reddening applied only to the youngest ages. Based on this SFH, we may only define an upper limit on the age of 4.5 Myr or less, corresponding to a mass of greater than  $52 M_{\odot}$ . The CMD displays no bright, blue upper MS stars, causing us to be suspicious of the extremely young progenitor star. In addition, the extended red clump indicates that differential reddening is not unique to the young stellar population.

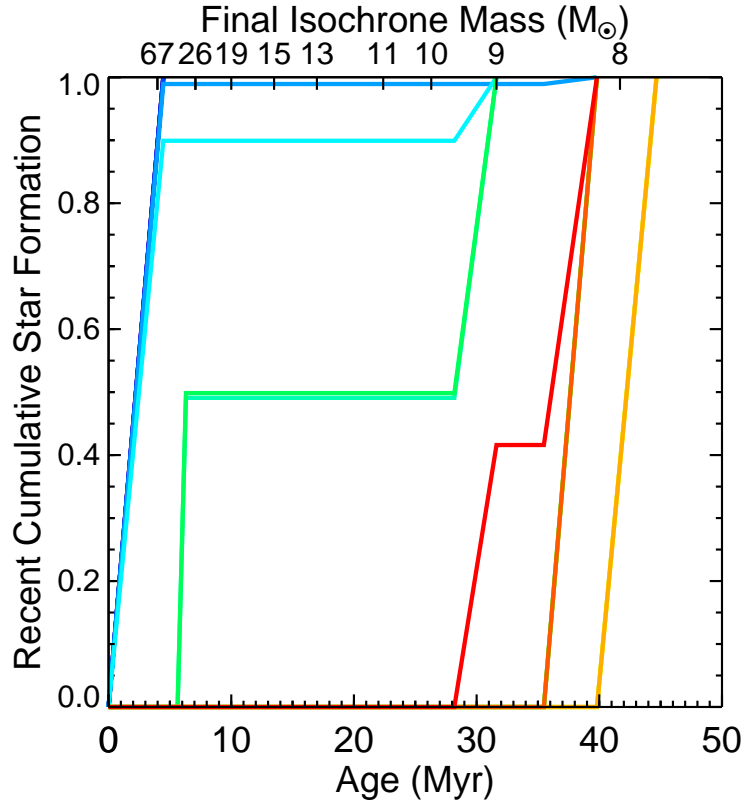


**Figure 4.** Cumulative star formation history for BW-102. Different lines correspond to different values of field-wide differential reddening, with blue lines corresponding to  $dA_v=0.0$  and redder lines corresponding to  $dA_v=1.5$ . This is in addition to the 0.5 magnitudes of  $dA_v$  applied by default to the young stellar population. Note that some lines are not visible because they find the exact same age as other lines, and therefore show up underneath other results. The red line was found to have the best fit while still maintaining a value above that of foreground reddening. It corresponds to an age of 36 Myr and a mass of  $8.5 M_{\odot}$ .

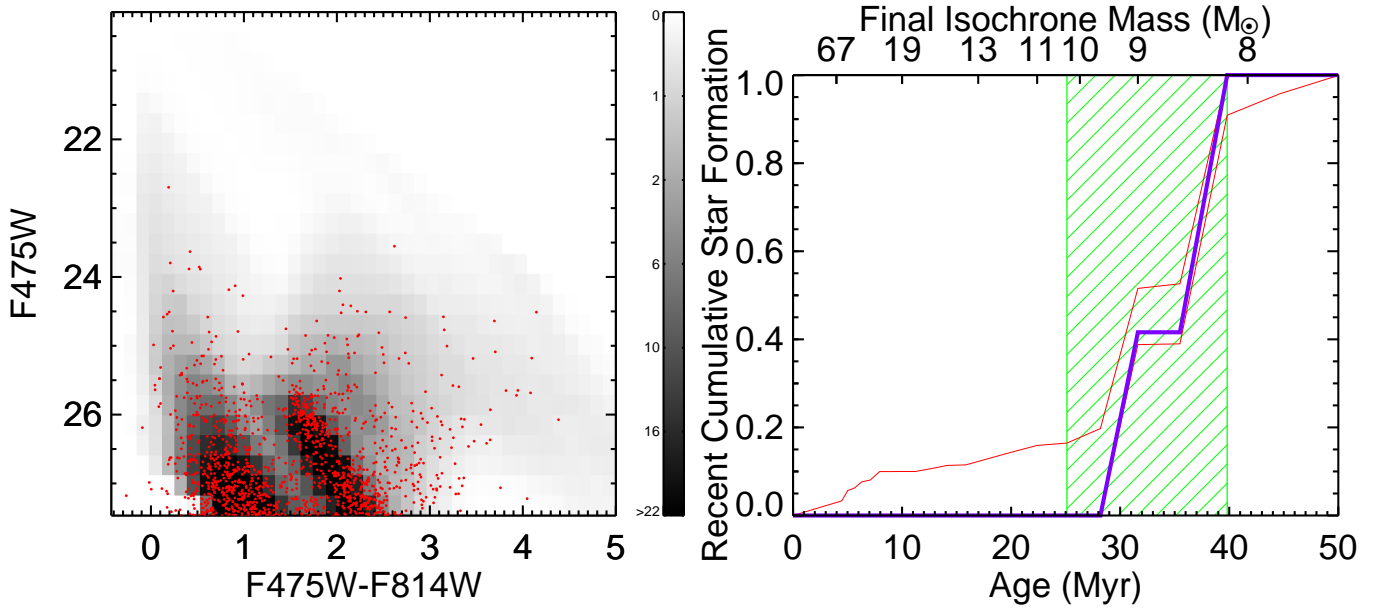


**Figure 5.** Left Panel: We plot the observed CMD of the region surrounding BW-102, plotted as magnitude in F475W vs. (F475W-F814W). We also plot the best-fit model created by MATCH in greyscale behind the observed CMD. The scale is printed to the right of the CMD. This model is found using the differential reddening procedure described in §2.4, leading us to use a value of  $dA_v = 0.5$ . Right Panel: Cumulative star formation over the most recent 50 Myr. We plot the best fit (purple line) with high and low errors as calculated by the Monte Carlo tests (red lines). The cross-hatched highlighted region is corresponds to our 16% to 84% confidence interval, which we define in §2.3. We find the data best fit by a burst of SF at  $36_{-11}^{+4}$  Myr, corresponding to  $8.5_{-0.5}^{+2.0} M_{\odot}$  (highlighted region).

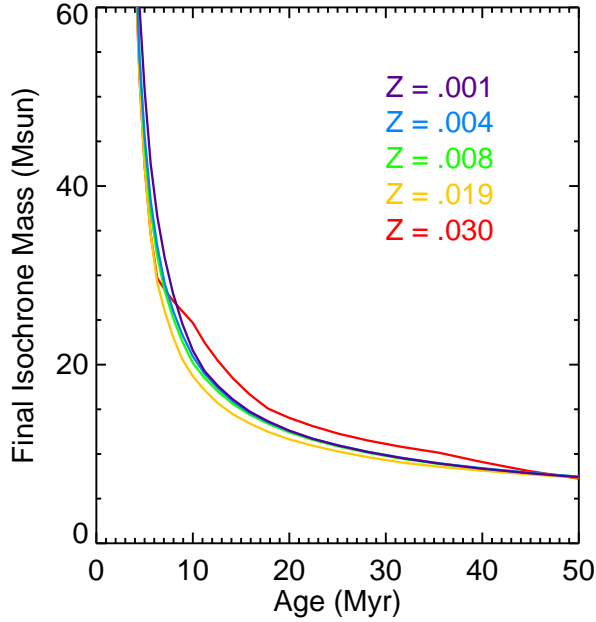


**Figure 6.** Marigo et al. (2008); Girardi et al. (2010) final isochrone masses plotted against isochrone age for metallicities of  $Z=0.004$ ,  $Z=0.008$ ,  $Z=0.019$  (solar), and  $Z=0.030$ . Based on the known gas-phase metallicity of M31 and our own best-fit metallicity values, we adopt solar metallicities for all age-to-mass conversions in this paper.

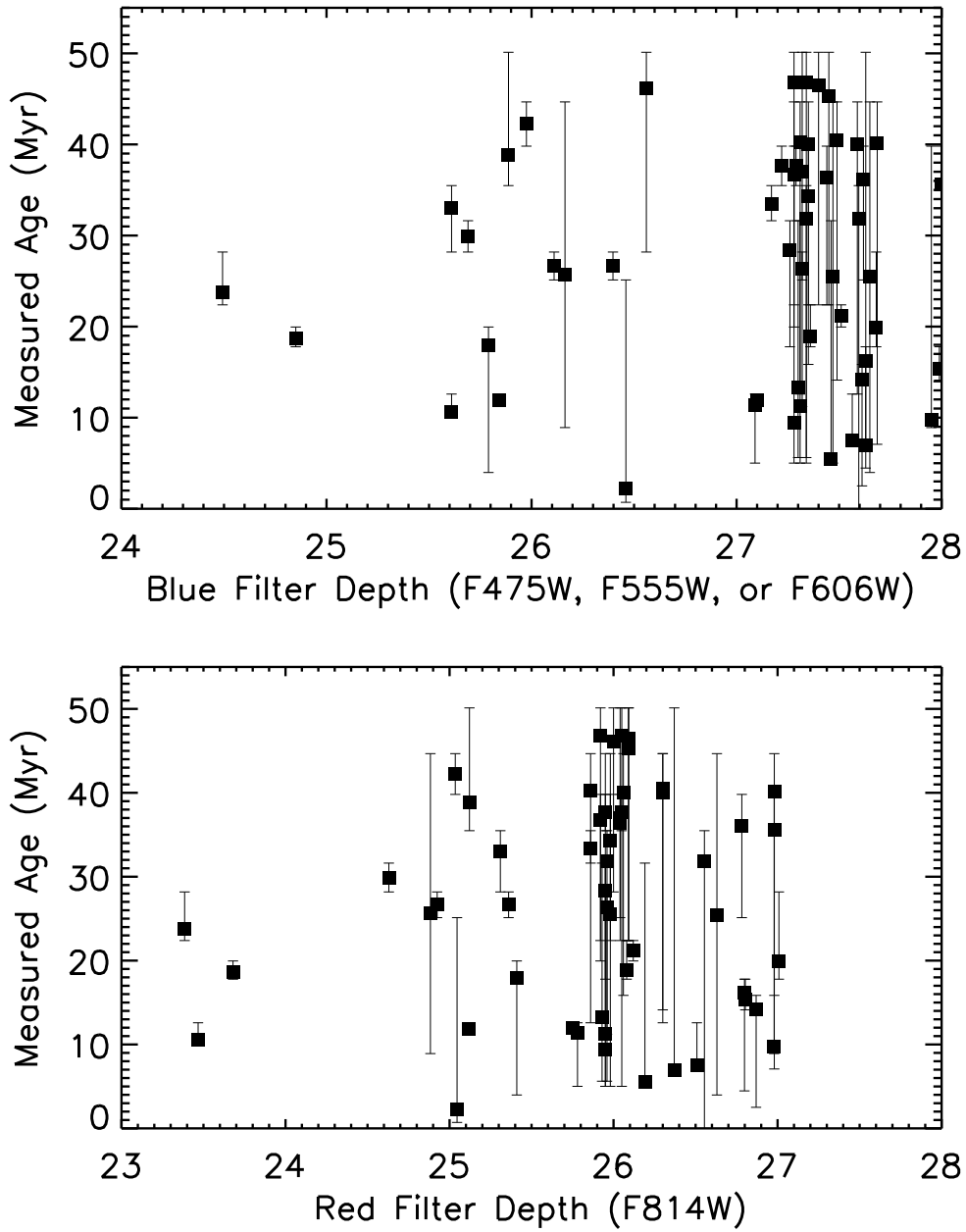


**Figure 7.** Top Panel: We plot the recovered ages for the progenitor stars against the 50% completeness limit for the redder broadband filter used. Bottom Panel: Same as top, but for the bluer filter used. The filter selection is somewhat arbitrary, since the bluer filter may be F475W, F555W, or F606W depending on the dataset. The redder filter will always be F814W. The data points do not include results for which no young SF was found. Following our depth cut, we find no significant correlation between depth in either filter and the measured age.

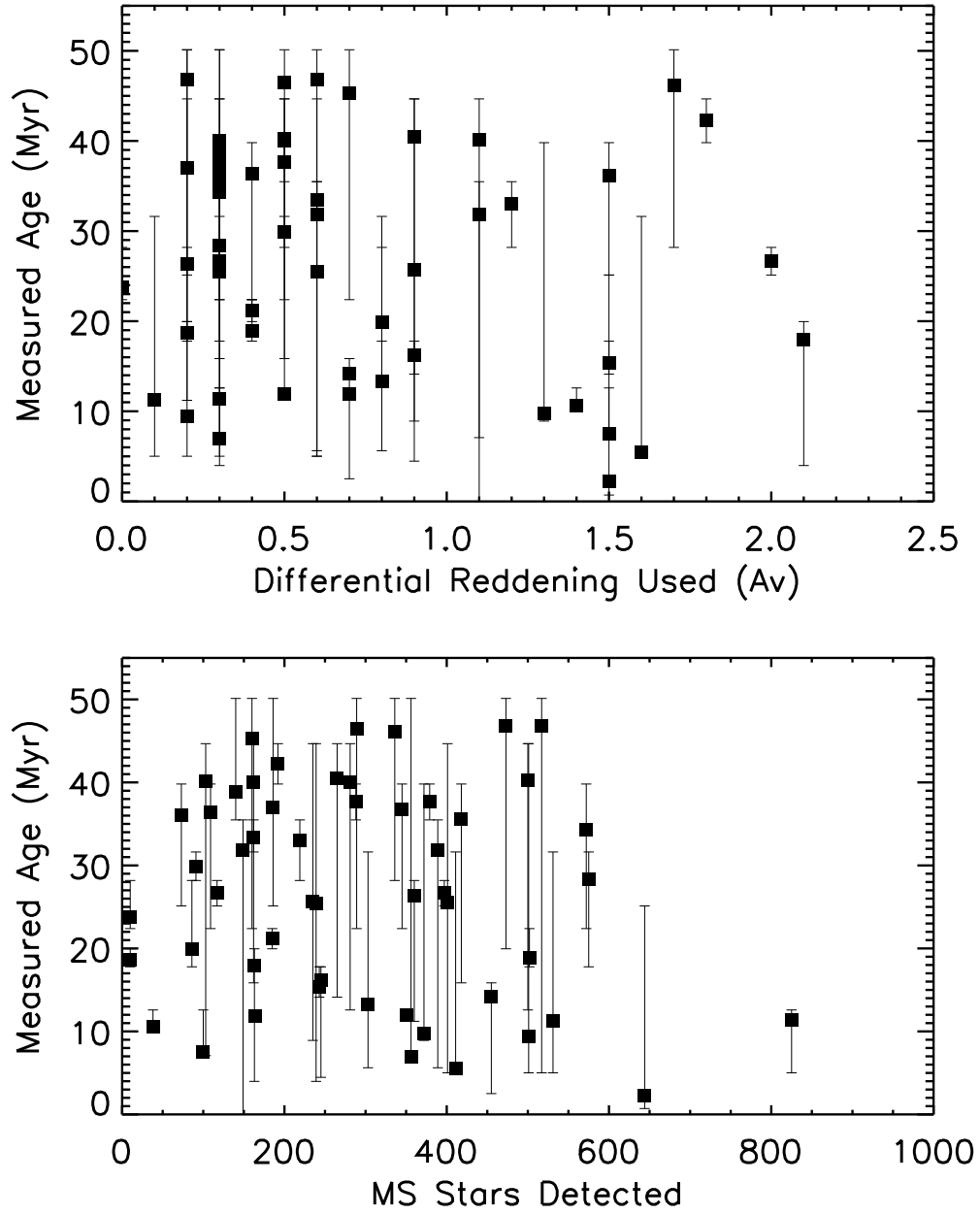


**Figure 8.** Top panel: We plot the recovered ages for the progenitor stars against the number of MS stars detected in the region around the SNR. Bottom panel: We plot the recovered ages against the value of  $dA_v$  used for ACS data only. These values include only the additional user-added  $dA_v$ , not the 0.5 mag of  $dA_v$  automatically included for young populations. The data points do not include results for which no young SF was found. We find no significant correlation between age and either  $dA_v$  or number of stars.

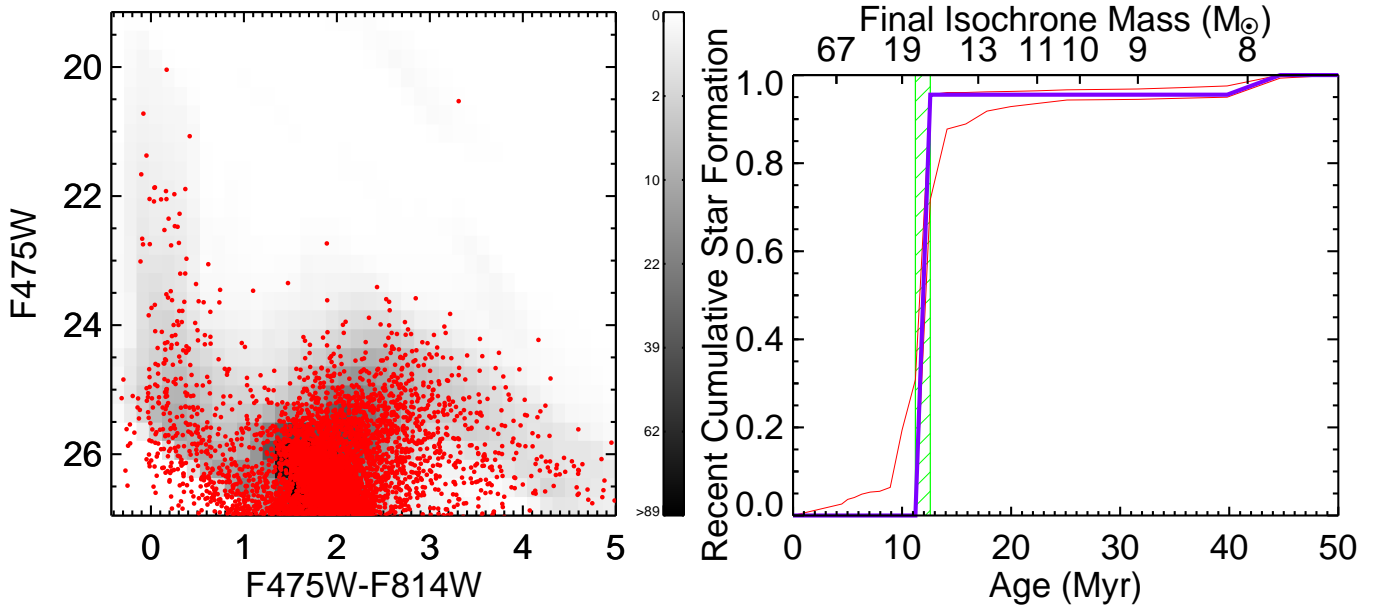


**Figure 9.** Left Panel: In red we plot the observed CMD of the region surrounding K376, plotted as magnitude in F814W vs. (F475W-F814W). We also plot the best-fit model created by MATCH in greyscale behind the observed CMD. The scale is printed to the right of the CMD. A prominent upper main sequence is clearly visible in the CMD, indicating a young stellar population and a more massive progenitor. Right Panel: Cumulative star formation over the most recent 50 Myr. We plot the best fit (purple line) with high and low errors as calculated by the Monte Carlo tests (red lines). The cross-hatched highlighted region is corresponds to our 16% to 84% confidence interval, which we define in §2.5. We find the data best fit by a single burst of SF at  $12 \pm 1$  Myr, corresponding to  $16 \pm 1 M_{\odot}$  (highlighted region).

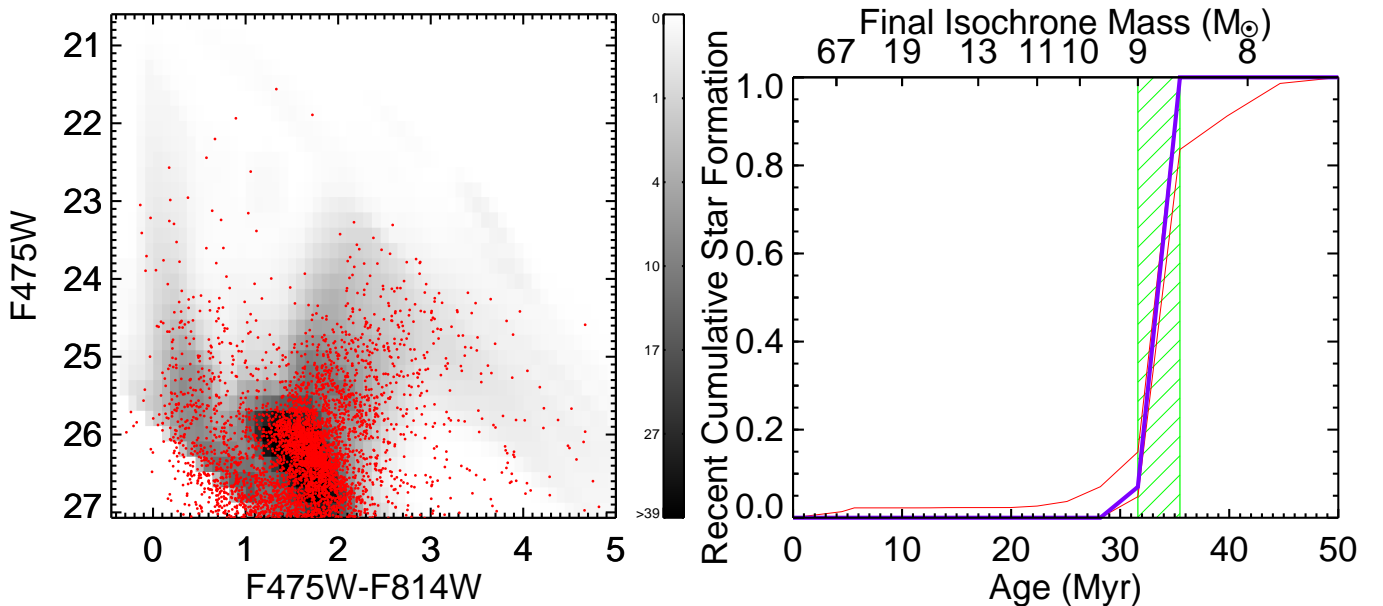


**Figure 10.** Same as Fig. 9, but for K180. Left Panel: In red we plot the observed CMD of the region surrounding K180, plotted as magnitude in F814W vs. (F475W-F814W). We also plot the best-fit model created by MATCH in greyscale behind the observed CMD. The scale is printed to the right of the CMD. The main sequence is dimmer than that for K376, indicating an older population and thus a less massive progenitor. Right Panel: Cumulative star formation over the most recent 50 Myr. We plot the best fit (purple line) with high and low errors as calculated by the Monte Carlo tests (red lines). The cross-hatched highlighted region is corresponds to our 16% to 84% confidence interval, which we define in §2.5. We find the data best fit by a single burst of SF at  $33 \pm 2$  Myr, corresponding to  $8.8 \pm 0.2 M_{\odot}$  (highlighted region).



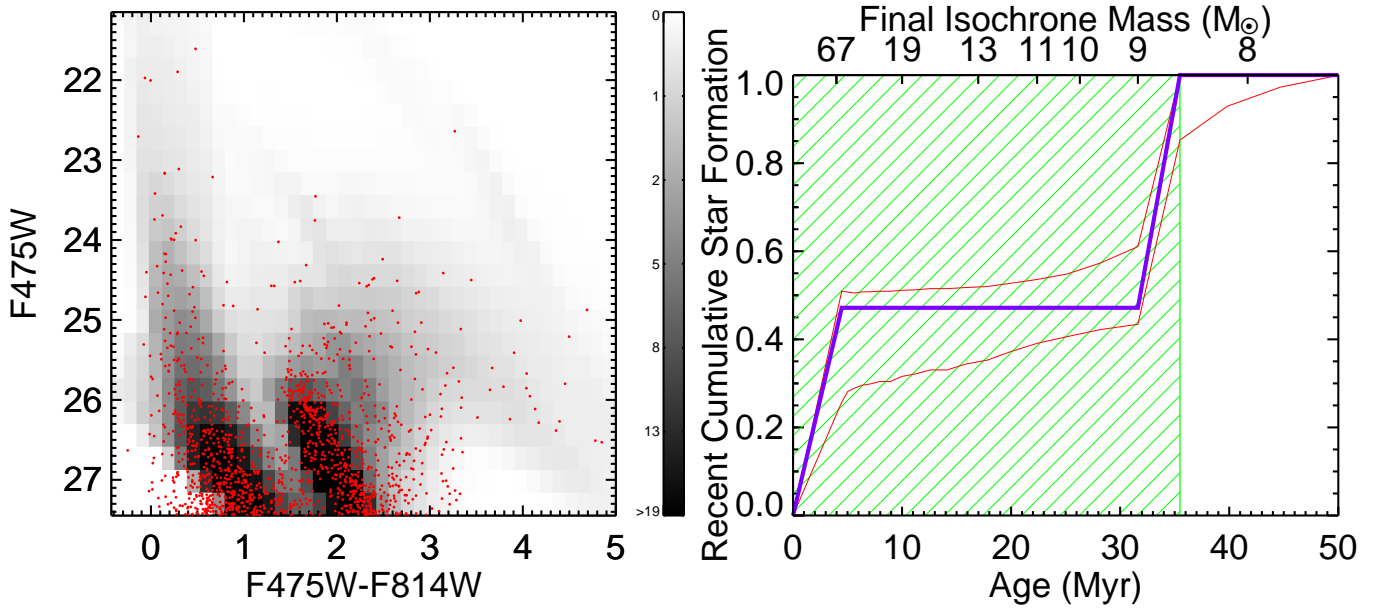


**Figure 11.** Same as Fig. 9, but for K891. Left Panel: In red we plot the observed CMD of the region surrounding K891, plotted as magnitude in F814W vs. (F475W-F814W). We also plot the best-fit model created by MATCH in greyscale behind the observed CMD. The scale is printed to the right of the CMD. Right Panel: Cumulative star formation over the most recent 50 Myr. We plot the best fit (purple line) with high and low errors as calculated by the Monte Carlo tests (red lines). The cross-hatched highlighted region is corresponds to our 16% to 84% confidence interval, which we define in §2.5. Unlike the previous examples, K891 seems to display two star formation events of similar prominence. We are unable to associate the progenitor star with either burst, and as such the only constraint we may offer is to say that the progenitor is younger than 36 Myr, corresponding to a mass of  $\geq 9 M_{\odot}$ .

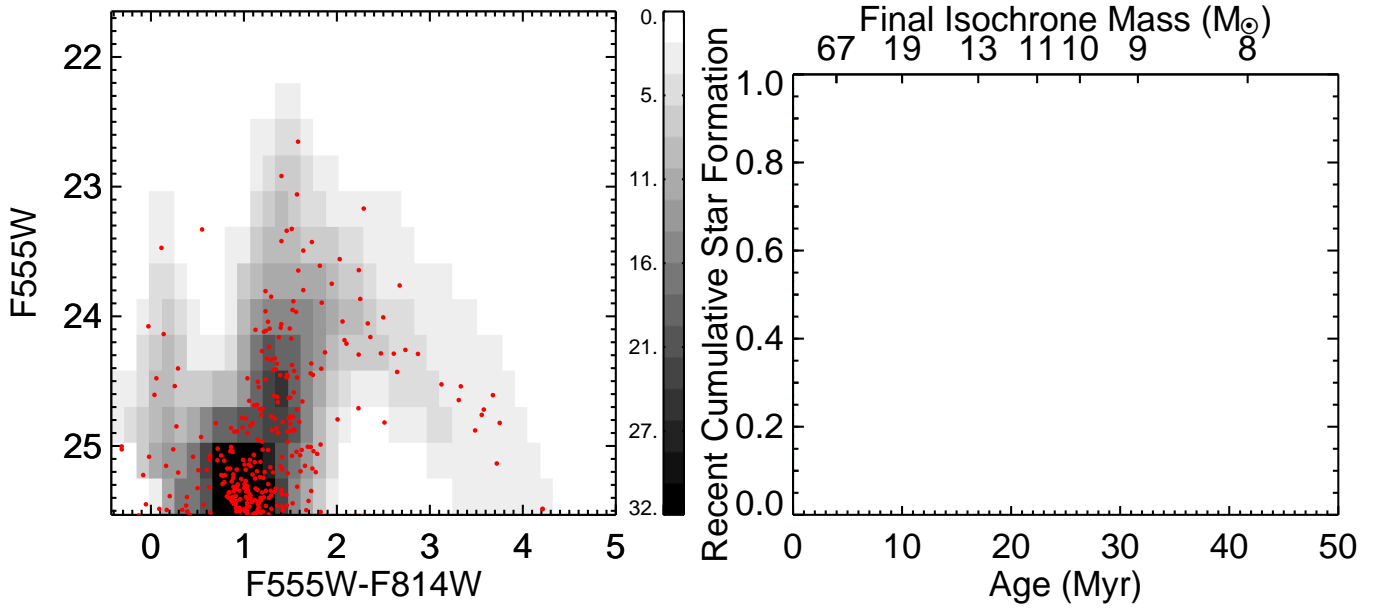


**Figure 12.** Same as Fig. 9, but for 2-028, with F555W instead of F475W. Left Panel: In red we plot the observed CMD of the region surrounding 2-028, plotted as magnitude in F814W vs. (F555W-F814W). We also plot the best-fit model created by MATCH in greyscale behind the observed CMD. The scale is printed to the right of the CMD. The main sequence is much dimmer than that for K376, indicating an older population and thus a less massive progenitor. Right Panel: Cumulative star formation over the most recent 50 Myr. We find no SF within the past 50 Myr for 2-028. We classify 2-028 as either a possible Type Ia remnant, or as a possible runaway star.

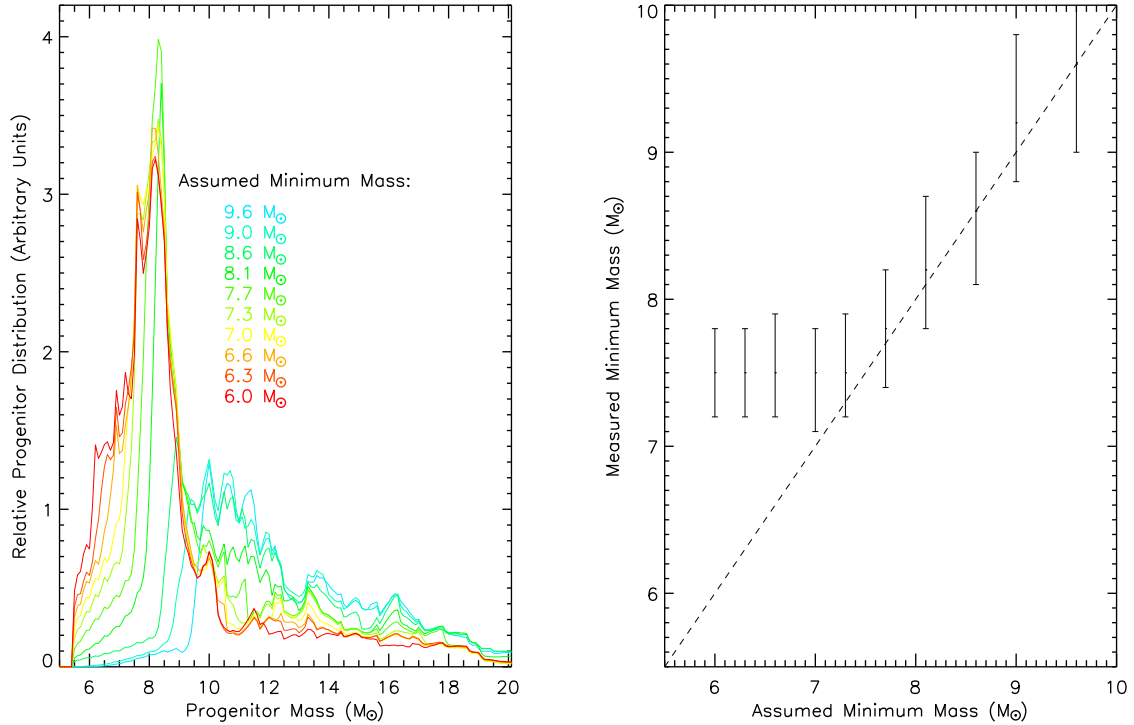


**Figure 13.** Left Panel: Plot of distribution of progenitor masses assuming different minimum mass for a star to undergo core collapse. We plot distributions for 6.0, 6.3, 6.6, 7.0, 7.3, 7.7, 8.1, 8.6, 9.0, and 9.6  $M_{\odot}$ . We note the existence of a large peak of masses located at  $\sim 8 M_{\odot}$ , which we argue represents the minimum core-collapse mass. We also note that this peak grows in size as we lower the minimum mass down to 7.3  $M_{\odot}$ , where it is constant. This suggests that we include the full number of progenitors when we include all star formation down to 7.3  $M_{\odot}$ , equivalent to the past 50 Myr of star formation. Right Panel: On the horizontal axis, we plot the minimum mass that we consider for purposes of determining recent star formation. On the vertical axis, we plot the corresponding mass for the largest value in the derivative of the progenitor mass distribution with respect to mass. We argue this spike represents the minimum mass for a star to undergo core-collapse. We find that above 7.3  $M_{\odot}$ , this value follows the assumed minimum mass. For 7.3  $M_{\odot}$  and below, this value remains at  $\sim 7.5 M_{\odot}$ . We assume that the precision with which we may define a value is  $\pm$  one age bin, and that the error bars on this minimum mass correspond to the final isochrone mass for these bins. Using this analysis, we find a range of values for the minimum mass from 7.0 to 7.8  $M_{\odot}$ .

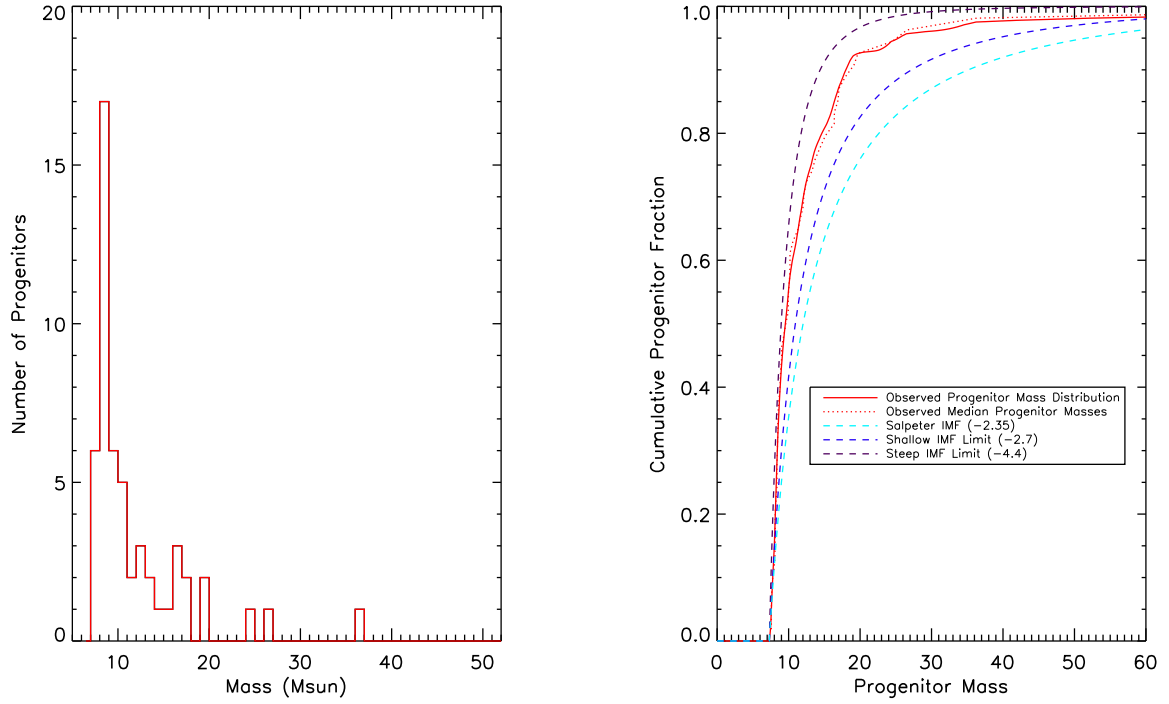


**Figure 14.** Left Panel: Histogram of median progenitor masses below  $52 M_{\odot}$ . Right Panel: Cumulative fraction of progenitor mass distribution. We overplot a reference Salpeter IMF. Using a KS-test, we find the cumulative mass distribution consistent with a power-law IMF of the form  $dN/dM \propto M^{\alpha}$  with  $-2.7 \geq \alpha \geq -4.4$ . We plot these two slopes, as well as a Salpeter IMF ( $dN/dM \propto M^{-2.35}$ ). While the distribution of masses greater than  $60 M_{\odot}$  is not shown, the fraction greater than  $60 M_{\odot}$  is given by the value for the cumulative fraction at  $60 M_{\odot}$ .

**Table 1** List of SNR with Deep 2-Filter HST Data

SNR ID	RA (degrees)	DEC (degrees)	HST Field	Project ID	Instrument	Filters w/ 50% Completeness Limits
Magnier et al. (1995) SNR						
1-006	10.6318	41.1005	POS-33	10273	WFPC-2	F555W=24.5, F814W=23.4
1-008	10.7675	41.6031	POS-21	10273	ACS	F555W=26.6, F814W=26.0
1-009	10.7975	41.6256	POS-23	10273	ACS	F555W=25.6, F814W=25.3
1-010	10.7979	41.4853	POS-18	10273	WFPC-2	F555W=24.9, F814W=23.7
2-016	10.3196	40.9554	G-87	6671	WFPC-2	F555W=25.2, F814W=23.9
2-020	10.4508	41.1138	G-104	10260	ACS	F606W=25.6, F814W=23.5
2-021	10.4773	40.7866	G-119	6671	WFPC-2	F555W=26.2, F814W=25.0
2-024	10.5958	41.0036	POS-29	10273	ACS	F555W=25.8, F814W=25.1
2-025	10.6448	40.9688	POS-29	10273	ACS	F555W=25.9, F814W=25.1
2-026	10.6698	41.0447	POS-30	10273	ACS	F555W=26.0, F814W=25.2
2-028	10.7376	40.9698	POS-41	10273	ACS	F555W=25.7, F814W=25.4
2-044	11.1989	41.4654	B08-F10	12075	ACS	F475W=27.3, F814W=26.0
2-046	11.2928	41.5993	B12-F17	12071	ACS	F475W=27.5, F814W=26.1
2-048	11.3094	41.6033	B12-F17	12071	ACS	F475W=27.5, F814W=26.1
2-049	11.3254	41.8683	B15-F08	12056	ACS	F475W=27.4, F814W=26.0
2-050	11.3662	41.8698	B15-F07	12056	ACS	F475W=27.4, F814W=26.1
Williams et al. (1995) SNR						
BW-11	10.2467	40.6081	G-76	11081	WFPC-2	F606W=26.2, F814W=24.9
BW-18	10.3988	41.1155	G-104	10260	ACS	F606W=26.1, F814W=24.9
BW-19	10.5408	40.9472	POS-27	10273	ACS	F555W=26.1, F814W=25.5
BW-20	10.5433	40.8644	POS-26	10273	ACS	F555W=26.0, F814W=25.0
BW-31	10.7317	40.9956	POS-41	10273	ACS	F555W=26.4, F814W=25.4
BW-32	10.7329	40.9717	POS-41	10273	ACS	F555W=25.7, F814W=24.6
BW-36	10.7725	41.3750	G-205	10260	ACS	F606W=25.5, F814W=24.5
BW-39	10.7933	41.6282	POS-23	10273	ACS	F555W=25.8, F814W=25.4
BW-44	10.8779	41.6882	POS-24	10273	ACS	F555W=26.5, F814W=25.0
BW-60	11.0883	41.9018	B15-F12	12056	ACS	F475W=28.0, F814W=26.8
BW-61	11.1054	41.3501	B06-F10	12105	ACS	F475W=27.3, F814W=25.9
BW-65	11.1488	41.4227	B06-F04	12105	ACS	F475W=27.3, F814W=25.9
BW-66	11.1550	41.8666	B15-F17	12056	ACS	F475W=27.5, F814W=26.2
BW-69	11.1825	41.9645	B17-F18	12059	ACS	F475W=27.6, F814W=26.5
BW-71	11.1958	41.4886	B08-F04	12075	ACS	F475W=27.5, F814W=26.0
BW-74	11.2129	41.4847	B08-F04	12075	ACS	F475W=27.1, F814W=25.8
BW-76	11.2267	41.5121	B08-F04	12075	ACS	F475W=27.3, F814W=25.9
BW-77	11.2269	41.5306	B08-F04	12075	ACS	F475W=27.3, F814W=25.9
BW-81	11.2858	41.6101	B12-F17	12071	ACS	F475W=27.4, F814W=26.1
BW-82	11.2892	41.8523	B15-F08	12056	ACS	F475W=27.6, F814W=26.3
BW-84	11.3162	41.6561	B12-F11	12071	ACS	F475W=27.4, F814W=26.0
BW-86	11.3387	41.6668	B12-F11	12071	ACS	F475W=27.3, F814W=26.0
BW-89	11.3650	41.9036	B15-F01	12056	ACS	F475W=27.5, F814W=26.3
BW-102	11.4675	42.1618	B21-F11	12055	ACS	F475W=27.6, F814W=26.8
BW-105	11.6296	41.9886	B18-F03	12108	ACS	F475W=27.6, F814W=26.6
BW-106	11.6417	42.1804	B21-F08	12055	ACS	F475W=28.0, F814W=27.0
BW-110	11.6896	42.2183	B21-F01	12055	ACS	F475W=27.7, F814W=27.0
Braun & Walterbos (1993) SNR						
K180	10.9186	41.1814	B02-F11	12073	ACS	F475W=27.2, F814W=25.9
K376	11.0850	41.5804	B09-F14	12057	ACS	F475W=27.1, F814W=25.8
K446	11.1298	41.3572	B06-F04	12105	ACS	F475W=27.3, F814W=26.0
K497	11.1562	41.4133	B06-F10	12105	ACS	F475W=27.3, F814W=26.0
K516/BW-67	11.1699	41.4145	B06-F04	12105	ACS	F475W=27.4, F814W=26.0
K525A	11.1820	41.4372	B08-F10	12075	ACS	F475W=27.3, F814W=26.0
K526A	11.1715	41.4653	B08-F10	12075	ACS	F475W=27.3, F814W=26.0
K527A	11.1834	41.4465	B08-F10	12075	ACS	F475W=27.3, F814W=26.0
K574	11.2101	41.4649	B08-F10	12075	ACS	F475W=27.4, F814W=26.1

**Table 1** List of SNR with Deep 2-Filter HST Data

SNR ID	RA (degrees)	DEC (degrees)	HST Field	Project ID	Instrument	Filters w/ 50% Completeness Limits
K594	11.2201	41.9161	B15-F10	12056	ACS	F475W=27.2, F814W=26.0
K856A	11.4313	41.9313	B16-F05	12106	ACS	F475W=27.6, F814W=26.4
K891	11.5405	42.2198	B21-F04	12055	ACS	F475W=27.6, F814W=26.6
K908	11.6231	41.9685	B18-F03	12108	ACS	F475W=28.0, F814W=27.0
K934/BW-107	11.6467	42.2266	B21-F01	12055	ACS	F475W=27.6, F814W=26.9
K947/2-047	11.6689	42.1911	B21-F07	12055	ACS	F475W=27.6, F814W=26.8
K956A	11.6792	42.2171	B21-F01	12055	ACS	F475W=27.7, F814W=27.0

Table 2 Progenitor Age and Mass Results

SNR ID	$M_{ZAMS}(M_{\odot})$	Age (Myr)	# MS Stars	Total Stars	Total Mass Formed( $10^2 M_{\odot}$ )	Additional $dA_v$ Applied
BW-74	$17^{+25}_{-2}$	$11^{+2}_{-7}$	825	4572	169	0.3
BW-44	$\geq 10$	$\leq 26$	644	2085	3	1.5
BW-86	$9.6^{+2.9}_{-0.6}$	$28^{+4}_{-11}$	575	4344	48	0.3
BW-84	$8.7^{+2.2}_{-0.6}$	$34^{+6}_{-12}$	572	5158	49	0.3
K527A	$17^{+25}_{-8}$	$11^{+20}_{-7}$	531	4925	62	0.1
2-049	$7.6^{+34}_{-0.3}$	$47^{+3}_{-42}$	517	4364	60	0.6
BW-81	$12^{+1}_{-2}$	$19^{+4}_{-2}$	502	5212	16	0.4
K525A	$20^{+22}_{-12}$	$9.4^{+35}_{-4.4}$	501	4677	121	0.2
BW-65	$8.1^{+7.6}_{-0.40}$	$40^{+4.4}_{-28}$	500	5263	57	0.5
BW-77	$7.6^{+4.1}_{-0.2}$	$47^{+3}_{-27}$	473	4968	31	0.2
K934	$\geq 13$	$\geq 16$	455	1934	75	0.7
K908	$8.6^{+4.9}_{-0.4}$	$36^{+5}_{-20}$	418	3360	47	0.3
BW-66	$36^{+6}_{-27}$	$5.5^{+26}_{-0.5}$	411	3310	63	1.6
BW-71	$10^{+32}_{-3}$	$25^{+19}_{-20}$	401	5281	37	0.6
BW-31	$9.9^{+0.3}_{-0.3}$	$27^{+2}_{-2}$	397	2288	23	0.3
K446	$9.0^{+26}_{-0.4}$	$32^{+4}_{-26}$	389	4921	26	0.6
K594	$8.4^{+0.2}_{-0.2}$	$38^{+2}_{-2}$	379	2537	26	0.5
BW-106	$19^{+2}_{-11}$	$10^{+30}_{-1}$	372	2642	64	1.3
K497	$10^{+7}_{-1}$	$26^{+2}_{-15}$	360	5106	26	0.2
K856A	$27^{+3}_{-19}$	$7^{+43}_{-1}$	356	2125	54	0.3
K376	$16^{+1}_{-1}$	$12^{+1}_{-1}$	350	6874	55	0.7
BW-76	$8.5^{+2.5}_{-0.3}$	$37^{+3}_{-14}$	345	5013	35	0.3
1-008	$7.6^{+2}_{-0.3}$	$46^{+4}_{-18}$	336	1895	61	1.7
BW-61	$15^{+20}_{-6}$	$13^{+18}_{-8}$	303	4835	106	0.8
2-050	$7.6^{+4}_{-0.3}$	$47^{+3}_{-24}$	289	4343	11	0.5
K526A	$8.4^{+0.2}_{-0.2}$	$38^{+2}_{-2}$	288	4842	3	0.3
BW-82	$8.1^{+8}_{-0.4}$	$40^{+5}_{-27}$	281	4017	8	0.3
BW-89	$8.1^{+7}_{-0.4}$	$40^{+5}_{-26}$	265	4296	43	0.9
K947	$13^{+39}_{-1}$	$16^{+2}_{-12}$	245	1874	37	0.9
BW-60	$14^{+1}_{-2}$	$15^{+3}_{-1}$	243	3277	39	1.5
BW-105	$\geq 8$	$\leq 44$	239	1945	13	0.3
BW-11	$10^{+10}_{-2}$	$26^{+19}_{-17}$	235	1199	105	0.9
1-009	$8.9^{+0.8}_{-0.3}$	$33^{+3}_{-5}$	219	739	36	1.2
BW-20	$7.9^{+0.3}_{-0.3}$	$42^{+3}_{-3}$	192	1339	22	1.8
2-044	$8.4^{+1.8}_{-1.1}$	$37^{+13}_{-12}$	186	4368	13	0.2
2-046	$11^{+1}_{-1}$	$21^{+2}_{-2}$	185	4445	16	0.4
2-024	$16^{+1}_{-1}$	$12^{+1}_{-1}$	164	1934	5	0.5
BW-39	$\geq 11$	$\leq 20$	163	844	104	2.1
K574	$8.1^{+6}_{-0.4}$	$40^{+5}_{-24}$	162	4207	18	0.5
K180	$8.8^{+0.2}_{-0.2}$	$33^{+2}_{-2}$	162	3950	23	0.6
2-048	$7.7^{+3.3}_{-0.4}$	$45^{+5}_{-23}$	160	3581	33	0.7
K891	$\geq 9$	$\leq 36$	149	1441	23	1.1
2-025	$8.2^{+0.4}_{-0.9}$	$39^{+11}_{-4}$	140	1287	13	0.3
BW-18	$9.9^{+0.5}_{-0.5}$	$27^{+2}_{-2}$	117	2165	25	2.0
K516	$8.5^{+3}_{-0.3}$	$36^{+4}_{-14}$	109	2210	10	0.4
K956A	$8.1^{+18}_{-0.4}$	$40^{+5}_{-33}$	103	1457	22	1.1
BW-69	$24^{+2}_{-9}$	$7.5^{+5}_{-1}$	100	1467	8	1.5
BW-32	$9.3^{+0.3}_{-0.3}$	$30^{+2}_{-2}$	91	562	6	0.5
BW-110	$12^{+1}_{-2}$	$20^{+8}_{-2}$	86	1391	12	0.8

**Table 2** Progenitor Age and Mass Results

SNR ID	$M_{ZAMS}(M_{\odot})$	Age (Myr)	# MS Stars	Total Stars	Total Mass Formed( $10^2 M_{\odot}$ )	Additional $dA_v$ Applied
BW-102	$8.5^{+1.5}_{-0.4}$	$36^{+4}_{-11}$	73	1568	31	1.5
2-020	$18^{+1}_{-2}$	$11^{+2}_{-1}$	38	1137	20	1.4
1-006	$11^{+1}_{-1}$	$24^{+5}_{-2}$	10	601	6	0.0
1-010	$12^{+1}_{-1}$	$19^{+2}_{-1}$	10	335	9	0.2
Fields with no recent SF (Probable Type 1a or Runaway Progenitors), not included in distribution						
BW-19	-	-	291	2520	0	0.5
BW-36	-	-	10	4162	0	1.3
2-026	-	-	191	2421	0	0.1
2-021	-	-	122	1268	0	0.0
2-028	-	-	53	374	0	0.5
2-016	-	-	5	466	0	0.6